

CONSTRAINING THE HIGH DENSITY NUCLEAR SYMMETRY ENERGY WITH PIONS

By

Justin Estee

A DISSERTATION

Submitted  
to Michigan State University  
in partial fulfillment of the requirements  
for the degree of

Physics – Doctor of Philosophy

2019

**ABSTRACT**

CONSTRAINING THE HIGH DENSITY NUCLEAR SYMMETRY ENERGY WITH PIONS

By

Justin Estee

Copyright by  
JUSTIN ESTEE  
2019

## **ACKNOWLEDGEMENTS**

Your acknowledgements here.

## TABLE OF CONTENTS

LIST OF TABLES . . . . .	vii
LIST OF FIGURES . . . . .	viii
CHAPTER 1 INTRODUCTION . . . . .	1
1.1 From Nuclear Forces to the Equation of State . . . . .	1
1.2 The Nuclear Equation of State . . . . .	1
1.3 Phases of Nuclear Matter . . . . .	1
1.4 Studying EoS through Heavy Ion Collisions . . . . .	1
1.5 Boltzmann Ulong Uhlenbeck (BUU) Transport Code . . . . .	2
1.6 Observables of interest to the EoS . . . . .	2
1.7 Pion Production . . . . .	2
1.8 Previous Constraints . . . . .	2
1.9 Motivation for building the S $\pi$ RIT TPC . . . . .	2
CHAPTER 2 EXPERIMENT . . . . .	3
2.1 Energy loss in material . . . . .	3
2.2 Pad Response Function . . . . .	3
2.2.1 Gatti Pad Response Function . . . . .	4
2.2.2 Experimental Pad Response Function . . . . .	4
2.3 Pad Response Function vs. crossing angle . . . . .	5
2.4 S $\pi$ RIT TPC Overview . . . . .	6
2.4.1 Enclosure . . . . .	9
2.4.2 Voltage Step Down . . . . .	9
2.4.3 Field Cage . . . . .	9
2.4.4 Voltage Step Down . . . . .	11
2.4.5 Wire Planes . . . . .	11
2.4.6 Pad Plane . . . . .	11
2.4.7 Electronics . . . . .	11
2.4.8 Considerations when constructing a TPC . . . . .	12
2.4.9 Gas Properties . . . . .	12
2.5 Ancillary Detectors . . . . .	14
2.5.1 Kyoto Multiplicity Trigger . . . . .	14
2.5.2 Krakow ?????? (KATANA) . . . . .	14
2.6 Radio Isotope Beam Factory (RIBF) Facility . . . . .	14
2.7 S $\pi$ RIT at RIBF . . . . .	15
2.8 Experimental Setup . . . . .	15
2.9 Trigger Condition . . . . .	15
2.10 Collision Data Taken . . . . .	16
CHAPTER 3 DATA ANALYSIS I: CALIBRATION AND CORRECTIONS . . . . .	17
3.1 Software . . . . .	17

3.2	Calibrations and Corrections . . . . .	20
3.2.1	Cocktail calibration . . . . .	20
3.2.2	Electronics calibration . . . . .	23
3.2.3	Anode gain calibration . . . . .	24
3.2.4	Extending the dynamic range of the Electronics . . . . .	25
3.2.5	Method of Desaturation . . . . .	28
3.2.6	Space Charge Corrections . . . . .	34
3.3	Monte Carlo Simulation . . . . .	44
3.3.1	Drift Task . . . . .	45
3.3.2	Pad Response Task . . . . .	45
3.3.3	Electronics Task . . . . .	46
3.3.4	Simulating Saturation . . . . .	46
3.4	Monte Carlo Track Embedding . . . . .	47
3.4.1	MC and Data Comparison . . . . .	48
3.5	Aligning TPC . . . . .	49
3.6	CoBo timing correction . . . . .	49
3.7	Efficiency Corrections . . . . .	49
3.8	Solid angle coverage . . . . .	50
CHAPTER 4 DATA ANALYSIS II . . . . .		51
4.1	Beam Particle Identification . . . . .	51
4.2	Edge Cuts . . . . .	51
4.3	High Density Cut . . . . .	51
4.4	Beam angle selection . . . . .	52
4.5	Vertex Cut . . . . .	52
4.6	Impact Parameter Selection . . . . .	55
4.7	Track Quality Cuts . . . . .	56
4.8	Angular Quality Cuts . . . . .	57
CHAPTER 5 RESULTS . . . . .		58
5.1	Comparison to Theory . . . . .	58
5.2	Pion Spectra and Yields . . . . .	58
5.3	$\pi^-/\pi^+$ Ratio . . . . .	58
5.4	Pion Double Ratio . . . . .	58
5.5	Pion Inferometry . . . . .	58
5.6	Constraint on the Symmetry Energy . . . . .	58
APPENDIX . . . . .		59
BIBLIOGRAPHY . . . . .		62

## LIST OF TABLES

Table 2.1	An overview of the properties of the S $\pi$ RIT TPC . . . . .	9
Table 2.2	Summary of range of GET electronics settings. . . . .	12
Table 2.3	. . . . .	13
Table 3.1	Summary of expected cocktail. . . . .	20
Table 3.2	Summary of expected cocktail. . . . .	21
Table 3.3	Summary of expected cocktail. . . . .	21
Table 3.4	Summary of expected cocktail. . . . .	21
Table 3.5	Summary of expected cocktail. . . . .	23
Table 3.6	Average energy loss of each beam. . . . .	34
Table 4.1	Summary of measured vertexes and their resolution. . . . .	53
Table .1	List of runs for the analysis. . . . .	60

## LIST OF FIGURES

Figure 2.1	Experimental pad response function of many events for a crossing angle of $85^\circ < \theta \leq 90^\circ$ . . . . .	5
Figure 2.2	Experimental pad response function as a function of the crossing angle $\theta$ with the corresponding fits. . . . .	6
Figure 2.3	Parameters $N_0$ and $\sigma$ as a function of the crossing angle $\theta$ with the 4 <sup>th</sup> order polynomial fits. . . . .	7
Figure 2.4	Exploded view of the S $\pi$ RIT TPC . . . . .	10
Figure 2.5	Drift velocity of electrons in P10 gas. . . . .	13
Figure 2.6	Number of electrons produced in a single avalanche on an anode wire. Two different voltages were simulated using Garfield++ at 1470 V and 1214 V. The expected Polya distribution fit is also given in yellow. . . . .	14
Figure 2.7	Overview of the RIBF, BigRIPS, and SAMURAI beamline. . . . .	15
Figure 3.1	Cartoon graphic of a top down view of a fit to a track passing through several pads. The bolded pads and the charges $q_i$ represent the hits belonging to that pad and the clusters of the track representing the average position of the track. The three clusters at the bottom are clustered in the x-direction and for the upper three clustered in the z-direction. The estimate of the position of the avalanche is given by the track fit and the position from the center to each pad to the $\bar{x}$ position is given as $\lambda_i$ . . . . .	19
Figure 3.2	A cartoon illustration of the charge distribution resulting from an electron avalanche on one wire and the projections of the distribution onto the two axis $\rho(x)$ onto the x-axis and $\rho(z)$ onto the z-axis. The orientation of the wire planes is flipped upside down to display the perspective better. . . . .	20
Figure 3.3	Calibration of electronics . . . . .	24
Figure 3.4	Calibration of low high. . . . .	25
Figure 3.5	The expected $dE/dx$ lines of different particles are given in red as calculated by Geant4. The approximate dynamic range of the TPC is shown by the vertical bar for the gain setting used in the experiment. Anything outside of this region would be saturated to some degree. . . . .	27

Figure 3.6	Cartoon of a top down view of a fit to a track passing through several pads. The bolded pads and the charges $q_i$ represent the hits belonging to that pad and the clusters of the track representing the average position of the track. The three clusters at the bottom are clustered in the $x$ -direction for the upper three are clustered in the $z$ -direction. The estimated position of the avalanche is given by the track fit, and the position from the center to each pad to the $\bar{x}$ position is given as $\lambda_i$ .	29
Figure 3.7	A typical case of a saturating event. The red pulses represent the time bucket signal for each collected charge. The pads directly underneath the avalanche point, $q_2'$ and $q_3'$ , are saturated while pads farther away, $q_1$ and $q_4$ are not saturated.	30
Figure 3.8	Pad plane projection for a cocktail event in the TPC.	31
Figure 3.9	Pad plane projection for a collision event in the TPC. Highlighted by red arrows are two regions of anode wires which had a reduced voltage of 1214 V. The voltage of the rest of the TPC anode wires are 1460 V. The reduction in voltage reduces the gain by a factor of about 10.	32
Figure 3.10	The left panel shows the high gain stopping power vs low gain when the method of desaturation was not applied. In the right panel the desaturation technique was applied to the high gain region. The low gain does not suffer from saturation and represents the true $dE/dx$ value.	33
Figure 3.11	Uncorrected (left panel) and desaturated (right panel) cocktail data.	33
Figure 3.12	Uncorrected (left panel) and desaturated (right panel) collision data at polar angles of $\theta < 40^\circ$ and azimuthal angles between $-80^\circ < \phi < 80^\circ$	34
Figure 3.13	Location of space charge in $^{132}\text{Sn}$	35
Figure 3.14	Beam path of the experiments	36
Figure 3.15	$\Delta V_x$ distribution for left-going and right-going tracks in the TPC for the	38
Figure 3.16	$\Delta V_{LR}$ as a function of the beam rate.	39
Figure 3.17	Space charge relation	40
Figure 3.18	Shift of tracks	41
Figure 3.21	A summary of all the effects modeled in the TPC MC simulation.	45
Figure 3.22	A cartoon of the wires over one pad.	46
Figure 3.23	Comparison of MC and data PRF	46

Figure 3.24 Pulse shapes for normal and saturated signals. Both are normalized to a max height of 1. . . . .	47
Figure 3.25 Comparison of MC to data. . . . .	49
Figure 3.26 Comparison of MC to data. . . . .	50
Figure 4.4 Distance to vertex for tracks. . . . .	57

# CHAPTER 1

## INTRODUCTION

### 1.1 From Nuclear Forces to the Equation of State

Isospin as a good quantum number at low energies Figure showing the nuclear forces for the pp, pn, nn Pauli exclusion inter particle distance , saturation density (maybe figure of all densities?) Building the infinite matter Statistical model Forces manifest in Energy/particle

### 1.2 The Nuclear Equation of State

Figure showing the binding energy vs p-n asym Liquid drop model, mass equation, move to higher densities Symmetric EoS asymmetric EoS(symmetry energy) Density dependence of the symmetry energy

### 1.3 Phases of Nuclear Matter

gas liquid phase, gas, where are we Progression through the heavy ion collision liquid, liquid gas, gas

### 1.4 Studying EoS through Heavy Ion Collisions

going from infinite matter to finite matter approximate nuclear matter with neutron rich radioactive ion beams probe different asymmetries probe different densities with different beam energies Symmetry energy goes down at higher beam energies

## **1.5 Boltzmann Ulong Uhlenbeck (BUU) Transport Code**

Does not reach equilibrium for all observable (hadrons) what about pions? Build up a mean field picture (momentum dependent) unknown quantities here Non equilibrium can be solved with Boltzman equation with collision term and solved by MC Figure of transport simulation code showing collision progression Clustering is an issue Meson, resonance production

## **1.6 Observables of interest to the EoS**

Particle yields of isospin opposites Flow?? Figure showing p-n observable lessens at high energy and from all densities

## **1.7 Pion Production**

Figure showing delta resonance Figure showing pion's produced at 2po Figure showing fermi motion effect (not really sub threshold but ok) (chemical potential model, delta isobar) prediction for pion ratio pion mass is small momentum shifted by coulomb affecting shape of pion spectra

## **1.8 Previous Constraints**

Figure showing GW constraint and other previous constraints FOPI data at 400 A MeV not as sensitive to symmetry energy Saturation density and lower constrained but issues at high density conflicting analysis on FOPI data which was not intended to be used for Symm Energy Can you group all the constraints to one nice plot???

## **1.9 Motivation for building the S $\pi$ RIT TPC**

Based on EOS TPC High efficiency for detecting pions and other light charged particles Effort to reduce the experimental error bars on such spectra which theory could use

## CHAPTER 2

### EXPERIMENT

#### 2.1 Energy loss in material

The average energy loss in a material can be described by the Bethe-Bloch equation,

$$\frac{dE}{dx} = \frac{4\pi N Z^2 e^4}{mc^2 \beta^2} \left( \ln \frac{2mc^2 \beta^2 \gamma^2}{I} - \beta^2 \right). \quad (2.1)$$

Where  $N$  is the number density of electrons in the medium,  $e$  the elementary charge,  $mc^2$  is the rest mass of the electron,  $Z$  is the charge of the traversing particle,  $I$  is the mean excitation energy of the medium, and  $\beta$  is the velocity of the particle. There is a large variation in energy loss around this mean value, with a long high energy loss tail. A full description of the energy loss distribution can be described in CITE HERE.

#### 2.2 Pad Response Function

The charge distribution on the pad plane resulting from an electron avalanche is two dimensional, as illustrated in Fig. 3.2, with the projections onto the  $x$  and  $z$  axis of this distribution labeled as  $\rho(x)$  and  $\rho(z)$  respectively. The charge observed on each pad is the integral of this distribution over the pad's dimensions, which is called the Pad Response Function (PRF).

In this example the clustering direction would be along the  $x$  axis, as illustrated by the bolded pads. By choosing to cluster only in one direction, we have not included the charge in adjacent pads along the  $z$  axis resulting from the tails of  $\rho(z)$ . Therefore the charge not included in the bolded pads will be incorporated into adjacent clusters, introducing small correlations in charge between neighboring clusters.

### 2.2.1 Gatti Pad Response Function

Gatti [1] derived a semi-empirical formula for the charge distribution in a simple multi-wire TPC. The function given in Eq. 2.2, depends only on the width of a pad ( $w$ ), the distance of the anode plane to the pad plane ( $h$ ), and the distance of the pad center to the avalanche point  $\lambda$ . It is a single parameter equation where the two parameters  $K_1 = \frac{K_2 \sqrt{K_3}}{4 \arctan(\sqrt{K_3})}$  and  $K_2 = \frac{\pi}{2} \left(1 - \frac{\sqrt{K_3}}{2}\right)$  depend on the parameter  $K_3$ , which is a function of the ratio of the anode wire diameter to the distance of the anode wires to the pad plane.  $K_3$  can be looked up in a graph in [2] and [1].

$$PRF_{\text{Gatti}}(\lambda) = \frac{K_1}{K_2 \sqrt{K_3}} [\arctan(\sqrt{K_3} \tanh[K_2(\frac{\lambda}{h} + \frac{w}{2h})]) - \arctan(\sqrt{K_3} \tanh[K_2(\frac{\lambda}{h} - \frac{w}{2h})])] \quad (2.2)$$

### 2.2.2 Experimental Pad Response Function

The correlations we introduced by only clustering along one direction do not play a significant role in the particle identification, but cause deviations from the expected Gatti distribution. Also, analytic PRFs only exist for classical multi-wire TPCs. For these reasons it is useful to experimentally measure the PRF and fit it with an empirical function, typically a Gaussian, to describe its behavior.

As in Fig. 3.6, we postulate that the PRF is a function of the total charge deposited in a cluster  $Q = \sum_i q_i$ , and the difference in position of the center of the  $i^{th}$  pad,  $x_i$ , to the mean position  $\bar{x} = \sum_i x_i q_i / Q$ , defined as  $\lambda_i = x_i - \bar{x}$ . The PRF is simply defined as the charge fraction of each pad as a function of  $\lambda$ , as shown in Equation 2.3.

$$PRF(\lambda_i) = \frac{q_i(\lambda_i)}{Q} \quad (2.3)$$

Averaging over many events in the experimental data, the resulting PRF for the S $\pi$ RIT TPC is shown in Fig. 2.1. Here we see the deviations from the expected analytic Gatti distribution (black curve), whereas fitting with a two parameter Gaussian function (red curve) gives a better

description of the data, Eq. 2.4, with the two parameters being the normalization coefficient,  $N_0$ , width  $\sigma$ , and with a mean value assumed to be 0.

$$PRF_{\text{Gaus}}(\lambda) = N_0 e^{\frac{-\lambda^2}{2\sigma^2}} \quad (2.4)$$

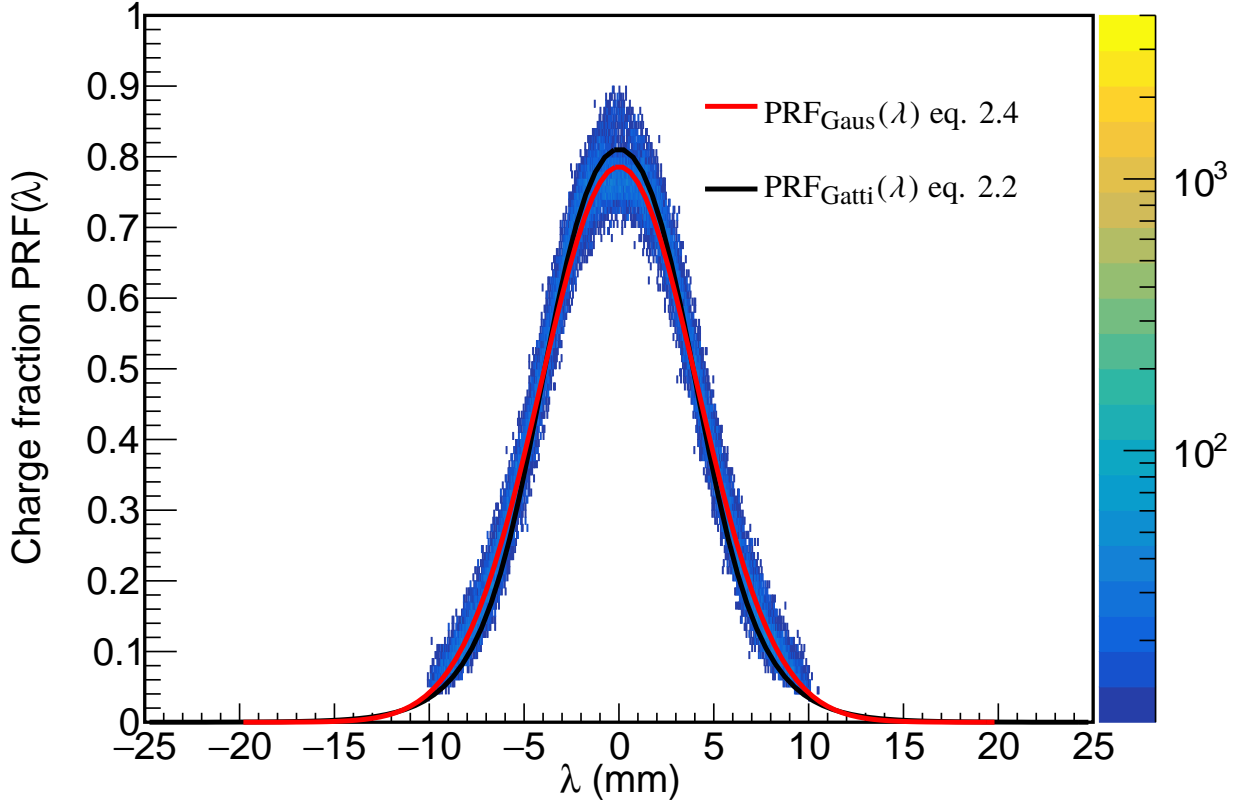


Figure 2.1: Experimental pad response function of many events for a crossing angle of  $85^\circ < \theta \leq 90^\circ$ .

### 2.3 Pad Response Function vs. crossing angle

The shape of the PRF depends on the crossing angle of the track [1]. Plotted in Fig. 2.2 is the PRF of  $\pi^-$  tracks vs. the crossing angle  $\theta$ . The PRF gets wider starting from  $90^\circ$  and going to  $45^\circ$ ; if we did not switch clustering directions the PRF would become wider until it was a uniform distribution and there was no position resolution. Since we switch the clustering direction from  $x$

to the  $z$  direction at  $45^\circ$ , the opposite trend is seen where the PRF becomes narrower as the position resolution gets better going from  $45^\circ$  to  $0^\circ$ .

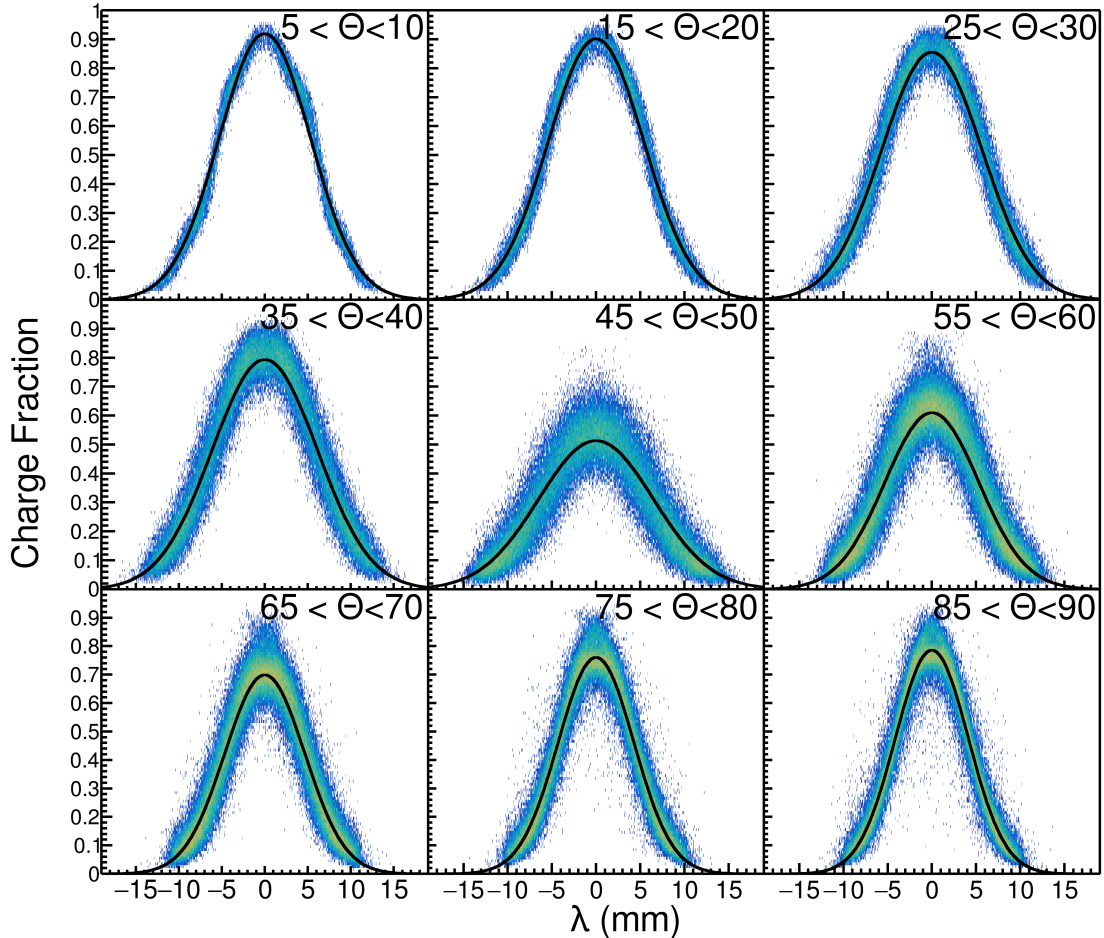


Figure 2.2: Experimental pad response function as a function of the crossing angle  $\theta$  with the corresponding fits.

Fits were performed to the experimental data with  $5^\circ$  width bins from  $0^\circ < \theta \leq 90^\circ$ . The two parameters of the Gaussian fits are plotted versus  $\theta$  in Fig. 2.3; a  $4^{th}$  order polynomial fit between these points allowed for interpolating between  $\theta$ .

## 2.4 S $\pi$ RIT TPC Overview

Add Overview image with labels

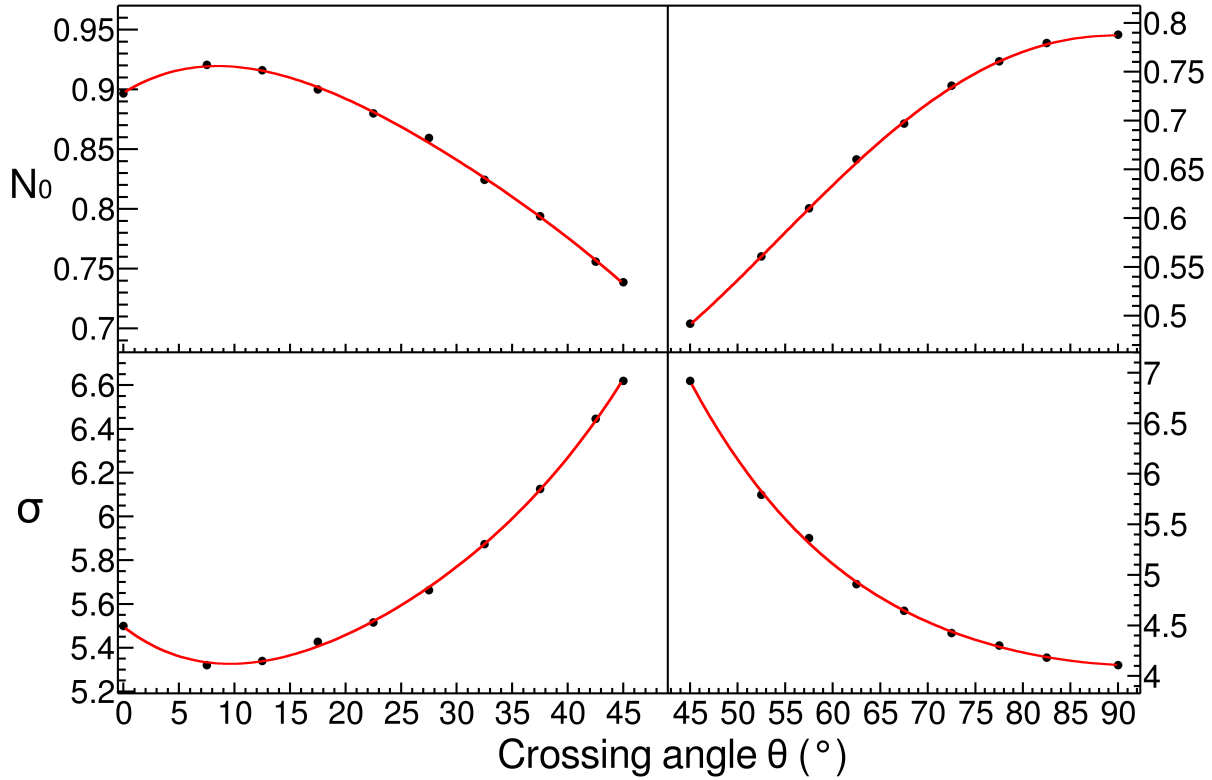


Figure 2.3: Parameters  $N_0$  and  $\sigma$  as a function of the crossing angle  $\theta$  with the 4<sup>th</sup> order polynomial fits.

The Samurai Pion-Reconstruction and Ion Tracker Time Projection Chamber (S $\pi$ RI TPC) is a Multi-Wire Proportional Counter developed to measure pions and other light charge particles resulting from radioactive heavy ion collisions in a fixed target experiments. The TPC is enclosed in a thin aluminum sheet walls all around in order to minimize neutron scattering and to allow for light charged particles to reach the arrays of scintillating bars detectors on the sides and downstream of the TPC. The S $\pi$ RI TPC was developed to fit inside the Samurai dipole magnet used at the Rare Isotope Beam Factory (RIBF) at RIKEN in Wako-shi, Japan [3]; the dipole gap limited the vertical space of the TPC. More detail and specifications of the Samurai dipole magnet are given in [4].

A target ladder allowed for up to 5 fixed targets to be mounted. A ACME worm gear allowed for the x-axis motion for changing the targets during the experiment, without needing to open or move the TPC. The motion of this worm gear was translated through the target motion feed-through

by several brass gears and non-magnetic gear boxes. The motion of the target ladder could be controlled by hand or by operation of the drill. The targets were mounted on stand-offs on the target ladder and also had z-axis motion. This allowed for the targets to be positioned as close as possible to the thin window of the field cage, maximizing the geometric acceptance.

The electronics were mounted to the aluminum top plate. Several aluminum ribs were mounted to the top of the plate to bring structural rigidity. A flatness within  $150\mu\text{m}$  was achieved across the whole top plate as measured by a laser position system. The charge sensitive pads of the pad plane were etched into several circuit boards were recessed and glued to the bottom portion of the top plate. Vias through the pad plane circuit boards brought the signal traces from the pads to surface mount pads on the other side of the boards. Several holes cut through the top plate allowed for the interface cables of the electronics to be connected to these surface pads.

Just below the pad plane were a set of three wire planes; the gating grid, ground, and anode wire planes. The detailed function of these wires will be explained later but they served to separate the boundary between the drift volume and the avalanche volume.

The front and sides of the field cage were assembled from 8 independent rigid circuit boards. The downstream window served as the downstream wall of the field cage all though it was a large polycarbonate frame in which a removable kapton window could be installed. This thin window minimized the scattering of exiting neutrons and charged particles for downstream detectors.

The voltage step down takes the high voltage of the field cage cathode and steps the voltage down through a set of copper rings and a resistor chain, minimizing the chance for sparking.

S $\pi$ RIT TPC Overview	
Pad plane area	1.3 m x .9 m
Pad size	1.2 cm x .8 cm
Number of pads	12096 (112 x 108)
Gas composition	90% Ar + 10% CH <sub>4</sub>
Multiplicity limit	200
dE/dx range	Z=1-8, $\pi$ , p,d,t,He,Li-O
Drift length	50 cm

Table 2.1: An overview of the properties of the S $\pi$ RIT TPC

#### 2.4.1 Enclosure

#### 2.4.2 Voltage Step Down

#### 2.4.3 Field Cage

The field cage was designed to hang from the top plate and therefore needed to be of a lightweight construction. Also the materials needed to be thin to allow for light charged particle and neutrons to pass through without significant scattering for ancillary detectors. Therefore instead of a downstream wall, a large thin exit window was constructed. The cathode was constructed of an aluminum honeycomb laminate. Two sheets of ??? aluminum were bonded to a core of aluminum honeycomb structure providing a lightweight yet rigid structure for the cathode.

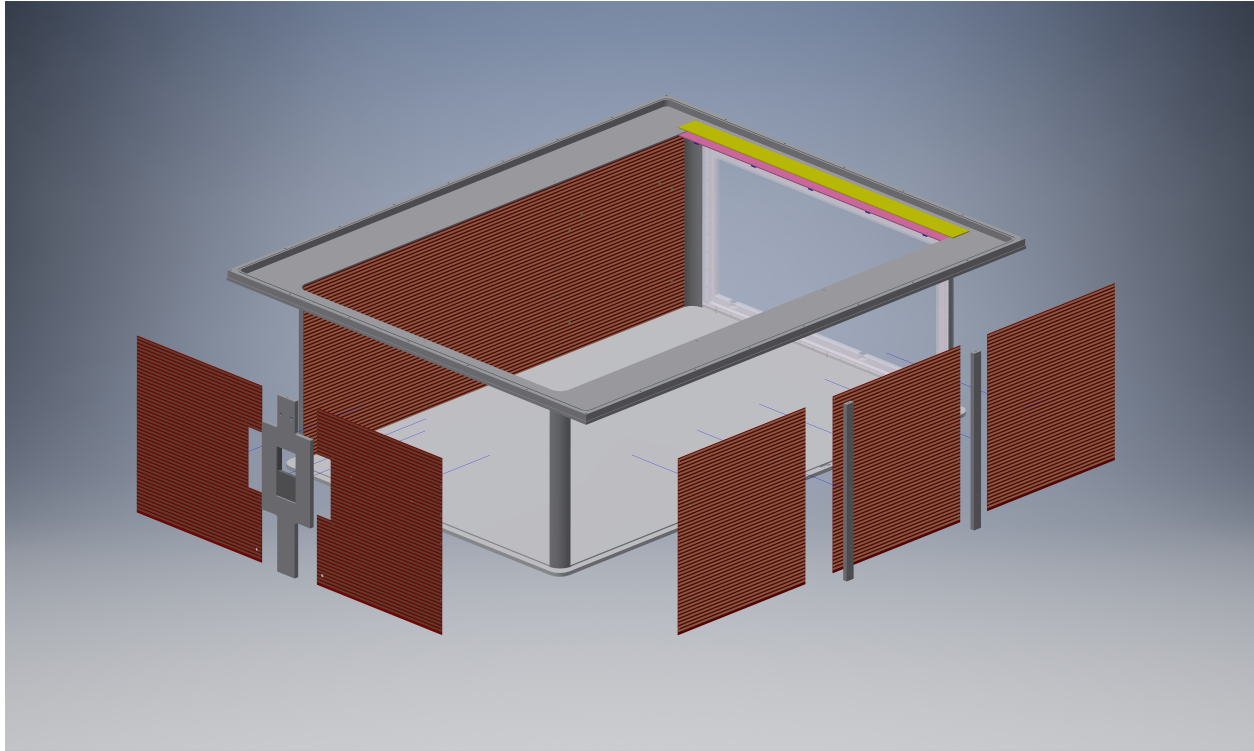


Figure 2.4: Exploded view of the S $\pi$ RIT TPC

The field cage was constructed from several panels of printed circuit boards (PCBs). The epoxy in the common PCB substrate FR4 contains bromine which is not suitable for the long term operation of a TPC, as the bromine will eventually cause gain reduction of the wires [CITE]. The halogen free material chosen was Rodgers ?????. We built the TPC with the option to run explosive gases such hydrogen, thus we decided to have field cage an isolated volume from the rest of the TPC enclosure. While the risk of a high voltage spark was minimized using the voltage step down, the risk of sparking when using an explosive gas could be further minimized by isolating the detector volume from the enclosure volume thereby allowing you to run an insulating gas between the field cage while running the explosive gas inside the detector volume only.

The front of the field cage was made of two PCBs and each side was constructed of three PCBs. The exit window was a  $10\mu\text{m}$  thick Kapton window with evaporated aluminum strips on the inside and outside; mounted on a polycarbonate frame.

#### **2.4.4 Voltage Step Down**

To lower the risk of a high voltage spark around the cathode region a voltage step down was developed. A series of 7 concentric copper rings with 20 M $\Omega$  resistors between them steps the cathode voltage down to ground. This minimizes sharp transitions of the electric field and therefore sparking.

#### **2.4.5 Wire Planes**

Add figure of gating grid transparency closed and open configuration

#### **2.4.6 Pad Plane**

Add figure of close up of pad plane

#### **2.4.7 Electronics**

Signals in the S $\pi$ RIT TPC are amplified and digitized by the recently developed Generic Electronics for TPCs (GET) [5]. Short cables transmit the signals from the pads to the inputs of the AGET chips. Each AGET chip services 64 pads (63 pads are connected in our case), contains a pre-amplifier, and a Switched Capacitor Array (SCA), with a maximum of 512 time buckets with an adjustable sampling frequency of 1 to 100 MHz. Four AGET chips are mounted on one AsAd (ASIC and ADC) motherboard. The gain of each AGET can be configured as 0.12, 0.24, 1.0, or 10 pC over the whole dynamic range, and the ADCs on each AsAd board provides 12 bit resolution. The peaking times of the shaping amplifiers can be set to 69, 117, 232, 501, 720, or 1014 ns. In this experiment, the gain was set to the highest setting, 0.12 pC, the peaking time 117 ns, and the sampling frequency 25 MHz (resulting in 40 ns time buckets). The Aget 2.0, asad 2.1, and cobo 1.0 firmware versions were used. The variations in the electronics were calibrated by measuring the response of each channel to a injected reference pulse, covering the full dynamic range of each channel.

GET electronics settings	
ADC bit range	14 bits
Sampling frequency	1-100 MHz
Dynamic range	.12, .24, 1.0, 10pC
Peaking time	69,117,232,501,720,1014 ns
Time bucket range	512

Table 2.2: Summary of range of GET electronics settings.

#### 2.4.8 Considerations when constructing a TPC

Several considerations went into the construction of the S $\pi$ RI TPC which I wish to summarize and document here. All materials and glues of the TPC were selected as low out-gassing materials. Several materials (that are common place in nuclear labs), such as vacuum grease, viton o-rings, all out-gas organic chemicals into the counter gas which damage the TPC by permanently lowering the gain over time. The organic molecules responsible are difficult to identify exactly, but lists of good and bad materials are well known in the literature from experiments. If a material we wished to use was not on these lists we placed the material in a clean chamber with the counter gas and flowed this counter gas through a small proportional counter making sure the gain did not drop at high collection rates when exposed to a high rate alpha Americium source.

Sparking Two volumes of gas.

#### 2.4.9 Gas Properties

$$\frac{d\vec{x}}{dt} = \frac{\mu}{1 + (\omega\tau)^2} \left( \vec{E} + \omega\tau \frac{\vec{E} \times \vec{B}}{|\vec{B}|} + \omega^2\tau^2 \frac{\vec{E} \cdot \vec{B}}{|\vec{B}|^2} \vec{B} \right) \quad (2.5)$$

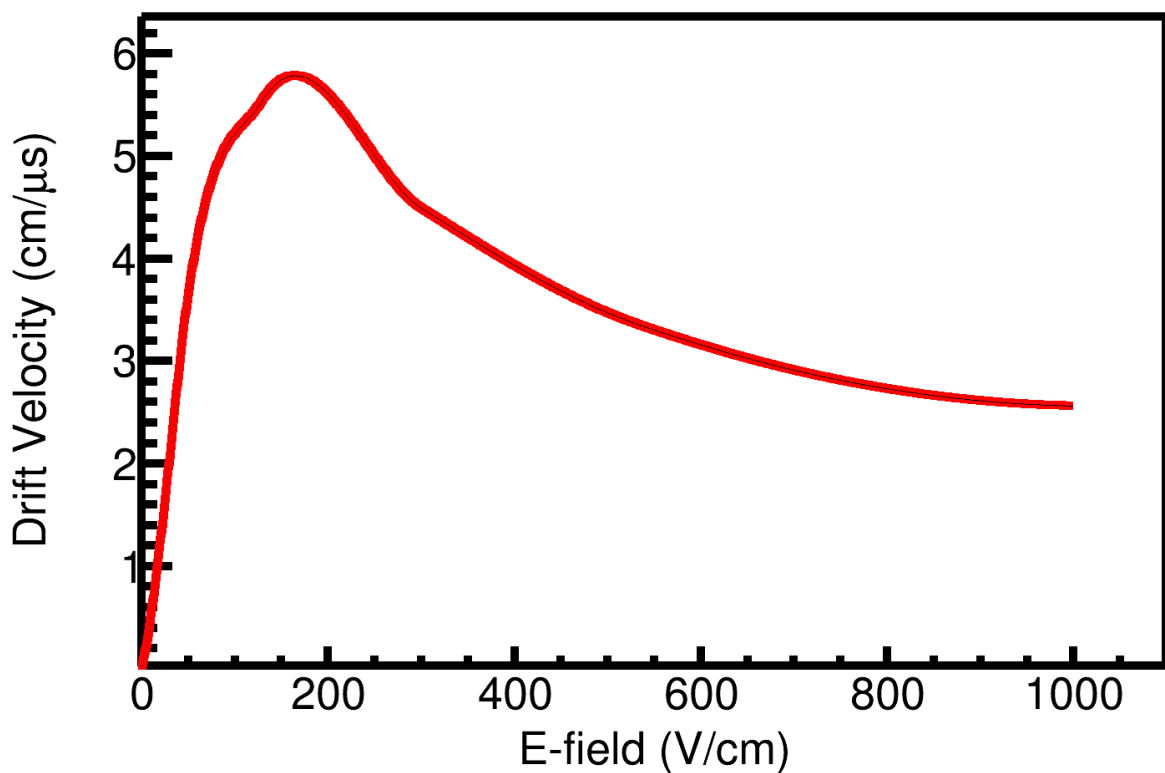


Figure 2.5: Drift velocity of electrons in P10 gas.

Gas properties	$\sigma_t$ (cm $^{-1/2}$ )	$\sigma_l$ (cm $^{-1/2}$ )	$v_d$ (cm μs $^{-1}$ )	$v_i$ (cm μs $^{-1}$ )	$G_h$	$G_l$
	0.024	0.034	5.43	$2.05 \times 10^{-4}$	903	150

Table 2.3

Add table for gas diffusion

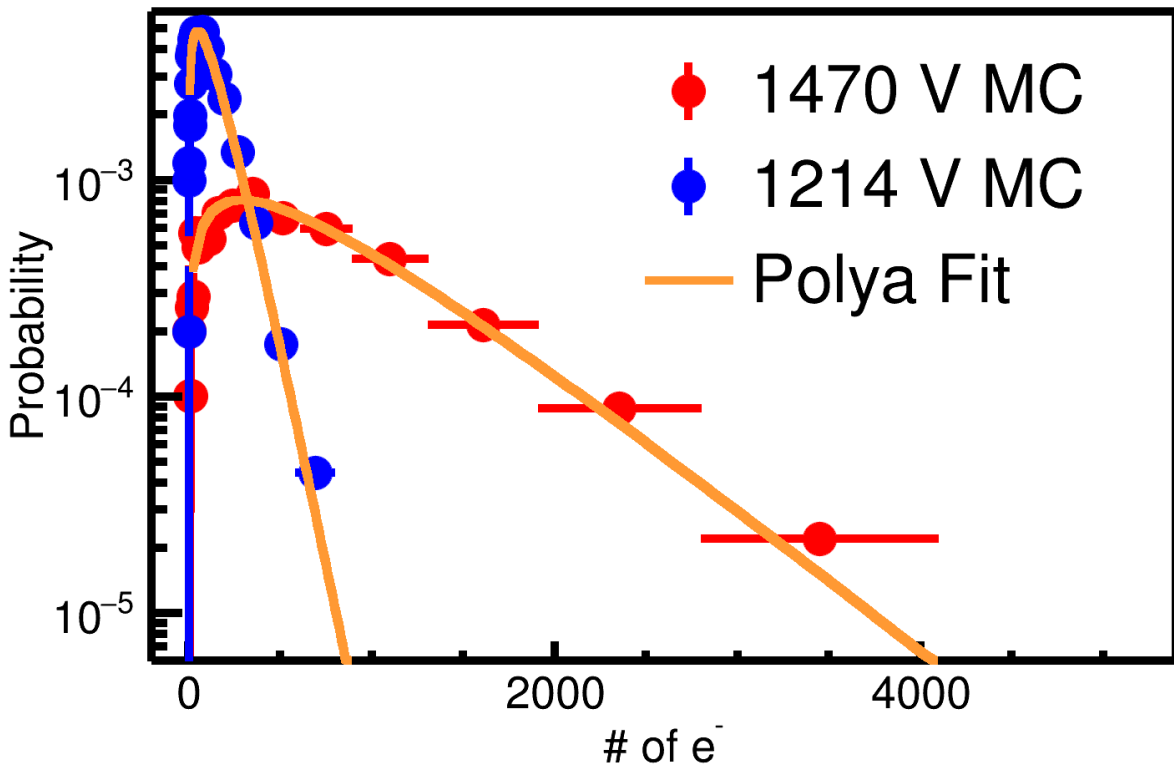


Figure 2.6: Number of electrons produced in a single avalanche on an anode wire. Two different voltages were simulated using Garfield++ at 1470 V and 1214 V. The expected Polya distribution fit is also given in yellow.

## 2.5 Ancillary Detectors

### 2.5.1 Kyoto Multiplicity Trigger

### 2.5.2 Krakow ?????? (KATANA)

## 2.6 Radio Isotope Beam Factory (RIBF) Facility

Cyclotron facility overview. Samurai line overview. Beam line element overview. Big rips beam PID. reference

## 2.7 S $\pi$ RIT at RIBF

Picture of setup.

SAMURAI (Superconducting Analyzer for Multi-particles from Radioisotope beams) is a large-acceptance multi-particle spectrometer for radioactive-beam experiments.

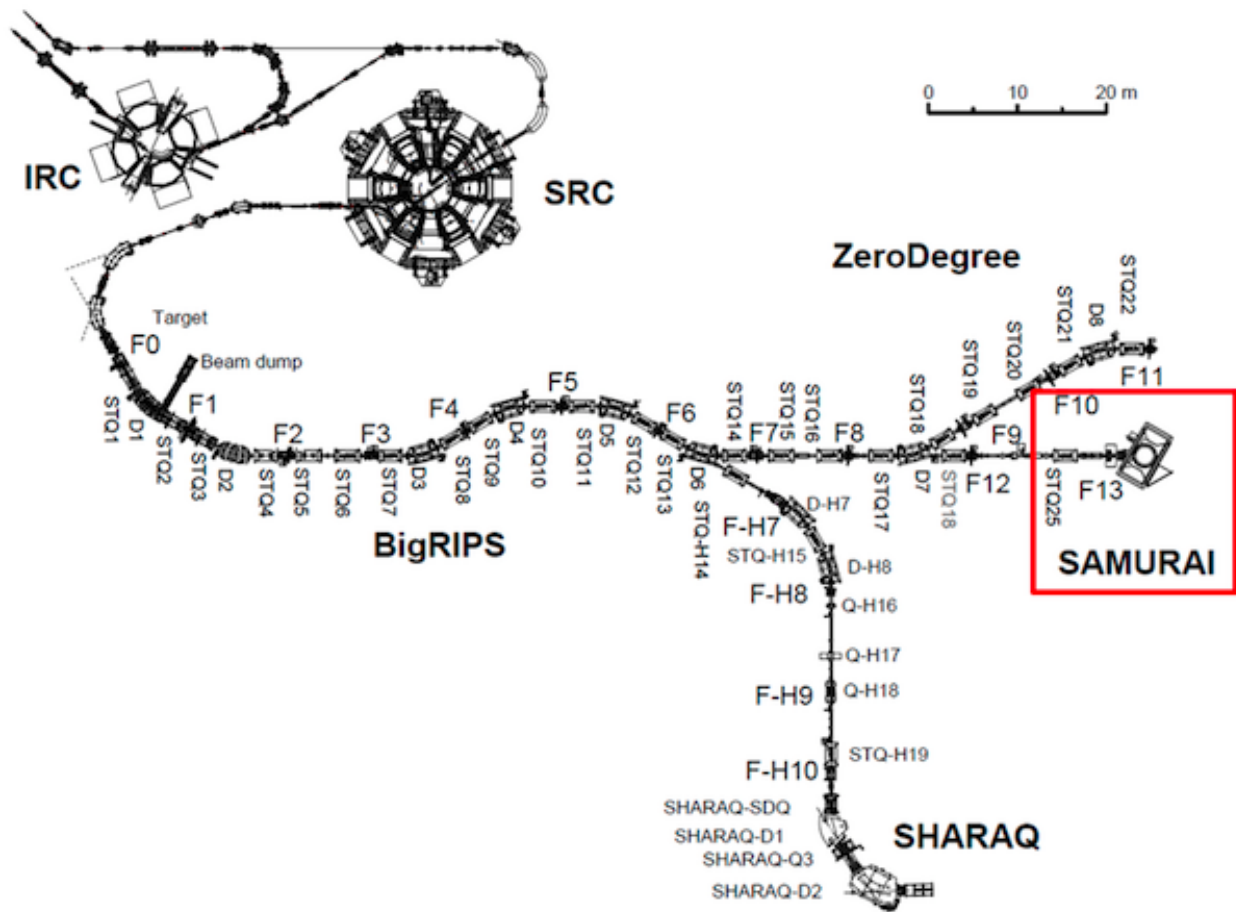


Figure 2.7: Overview of the RIBF, BigRIPS, and SAMURAI beamline.

## 2.8 Experimental Setup

### 2.9 Trigger Condition

How it was made using kyoto krakow

## **2.10 Collision Data Taken**

## CHAPTER 3

### DATA ANALYSIS I: CALIBRATION AND CORRECTIONS

Need to explain pedestal subtraction GG noise subtraction

#### 3.1 Software

The S $\pi$ RITROOT software is modular task based code based on the FAIRROOT package written in C++ [6]. The main tasks in the S $\pi$ RITROOT software reconstruction are:

- Decoder task
- Pulse Shape Algorithm (PSA Task)
- Helix Track Finding Algorithm
- Clustering Algorithm
- Track Fitting (GENFIT package)
- Vertex Fitting (RAVE package)

The decoder task converts the binary data file into a container class which maps the electronics channels into the corresponding pads and (x,z) coordinates.

There may be several pulses in a pad coming from two tracks passing under the same pad separated by arrival time. Using an expected pulse shape the PSA task fits the signal pulses within a pad, giving the arrival time of the drifted electrons from each particular track. The height of the fitted pulse is proportional to the total charge of that event, Q and the y-coordinate is calculated as  $y = v \cdot t_0$  where  $v$  is the drift velocity and  $t_0$  the arrival time. Combining the information from these first two tasks, (x,y,z,Q), we construct what is called a "hit".

The Helix Track Finding Algorithm finds the collection of hits belonging to one track out of all the hits in an event. The hits within a track are then reduced into clusters. A cluster's position is

the average position of the hits within a cluster, with the total charge of the cluster being the sum of the hits charges.

A tracks average position is estimated by the cluster's average position. The clusters are then fitted in the GENFIT track fitting package [7], giving the final momentum of the track. A final vertex of the event is fitted from all tracks using the package RAVE [8].

**Definition of clustering** A brief description of the method of clustering is illustrated in Figure 3.6. It is impractical to cluster in both the x and z-axis and we only cluster the hits along one axis. The three clusters at the bottom of Figure 3.6 are clustered along the x-axis and the upper three are along the z-axis, as shown by the bolded pads for one of the clusters in each direction.

The clustering direction depends on the angle of the track with respects to the x-axis, defined as  $\theta$ . For example, a track going along the z-axis the crossing angle is defined as  $90^\circ$ , and a track going along the x-axis defined as  $0^\circ$ . In the case that the crossing angle is  $45^\circ < \theta \leq 90^\circ$  the clustering direction is along the x-axis. For  $0^\circ < \theta \leq 45^\circ$  it is along the z-axis.

The position along the clustering direction is calculated by weighting the individual hit's positions by their charges  $q_i$  and getting the mean value. The other direction is set to the center of the pad. For example if we are clustering along the x-axis for a cluster, the z-position is set to the center of the pad in the z-direction and vice versa.

Clustering in this way gives us better position resolution for calculating the position of each cluster. You could imagine if we calculated the clusters only along the x-axis for tracks with  $\theta \approx 0^\circ$  the x-position is not well defined. By clustering in the direction most perpendicular to the track, we get a better position resolution.

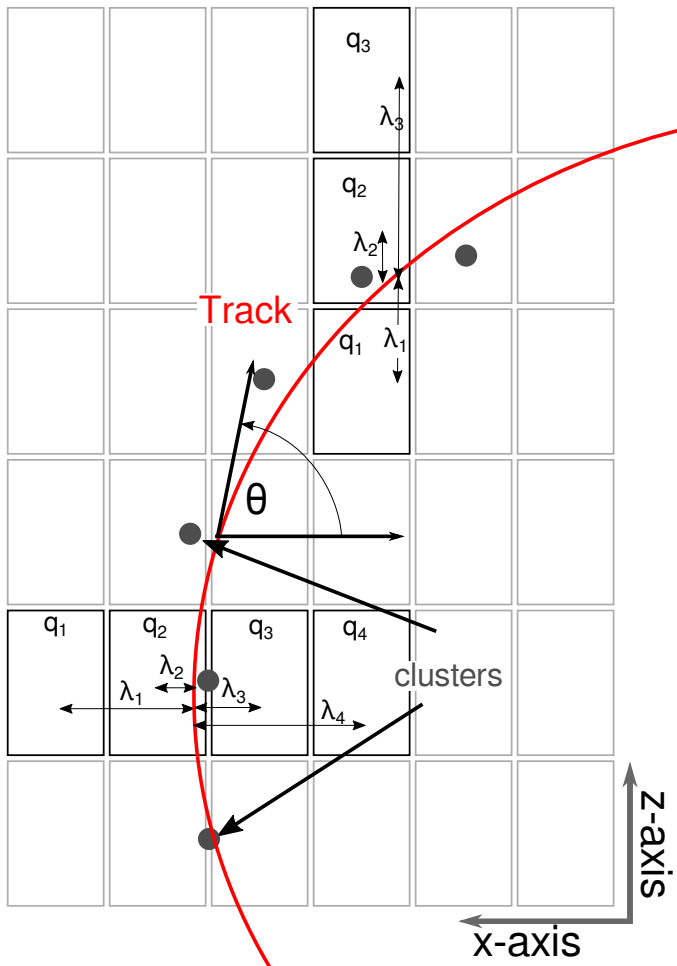


Figure 3.1: Cartoon graphic of a top down view of a fit to a track passing through several pads. The bolded pads and the charges  $q_i$  represent the hits belonging to that pad and the clusters of the track representing the average position of the track. The three clusters at the bottom are clustered in the x-direction and for the upper three clustered in the z-direction. The estimate of the position of the avalanche is given by the track fit and the position from the center to each pad to the  $\bar{x}$  position is given as  $\lambda_i$ .

100MeVTarget					
Particle	Measured	Corrected	% Difference	% Difference	
p	882.8	929.5	877.3	3.7	-1.0
d	817.1	831.15	797.94	1.7	-2.3

Table 3.1: Summary of expected cocktail.

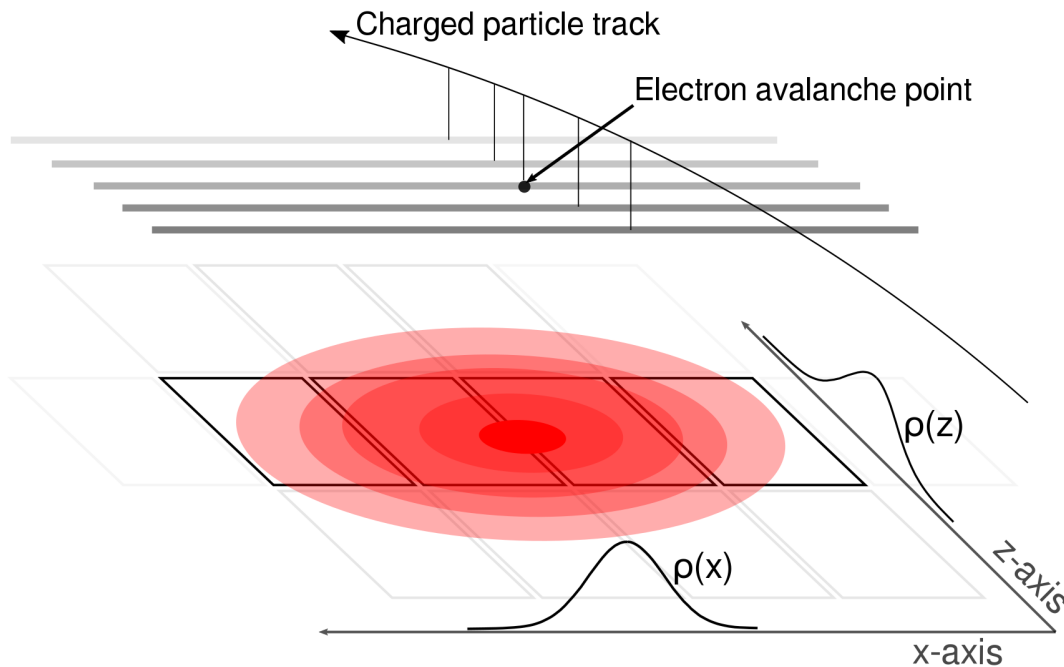


Figure 3.2: A cartoon illustration of the charge distribution resulting from an electron avalanche on one wire and the projections of the distribution onto the two axis  $\rho(x)$  onto the x-axis and  $\rho(z)$  onto the z-axis. The orientation of the wire planes is flipped upside down to display the perspective better.

## 3.2 Calibrations and Corrections

### 3.2.1 Cocktail calibration

Light charged particles ( $p, d, t, {}^3\text{He}, {}^4\text{He}$ ), beams were produced and measured in the TPC. The magnetic and slit settings of the dipoles in the BIGRIPS spectrometer was set so that the measured

100MeV						
Particle	Expected	Measured	Corrected	% Difference	% Difference	
p	882.8	903.5	889	2.0	-1.6	
d	817.1	898.5	874.5	2.1	-2.7	

Table 3.2: Summary of expected cocktail.

300MeV						
Particle	Expected	Measured	Corrected	% Difference Raw	% Difference	Corrected
d	1621	1704	1612	5.1	-0.6	
t	1612	1691	1596	4.9	-1.0	
<sup>4</sup> He	1613	1698	5.3	1595	-1.1	

Table 3.3: Summary of expected cocktail.

Particle	100MeV				100MeV				300MeV	
	Measured				Measured				Measured	
	Measured	E×B	Measured	E×B	Measured	E×B	Measured	E×B	Measured	E×B
p	882.8	929.5	877.3	903.5	929.5	889			f	f
d	817.1	831.15	d	898.5	e	e	1621.1	1704	1612	
t	589.5	d	d	887	e	e	1612.4	f	f	
<sup>3</sup> He	1617.3	d	d	1795.2	e	e	3236.4	f	f	
<sup>4</sup> He	1405.6	d	d	1782.9	e	e	3226.4	f	f	

Table 3.4: Summary of expected cocktail.

momentum resolution of the beam was  $\frac{\delta p}{p} < 1\%$ . Two magnetic rigidity settings were studied, with an empty target. A thick Aluminum target was used to provide a slightly lower point for part of the lower rigidity setting, effectively creating three calibration points over several particle species. The production of certain particles ( $t, {}^3He$ ), produced too few counts to make a good measurement, and in the high momentum rigidity setting protons could not propagate down the line and there were no counts.

Since the expected momentum resolution resulting from the spectrometer was less than 1%, the observed momentum resolution measured by the TPC is a good measurement of the combined momentum resolution of the software and TPC (intrinsic detection) system. The momentum resolution of the TPC depends on several factors such as the particle's angle, momentum, charge, track multiplicity, etc. This calibration beam represents an ideal situation where the track was parallel to the pad plane and only one particle was measured at one time. The energy loss resolution can also be directly inferred from the measurement since each energy setting represents a monochromatic source of each particle species, which has a well defined energy loss distribution. An average momentum resolution of 2% and the energy loss resolution of 5% was measured for particles ranging from protons to  ${}^4He$ , over the range of momenta measured in the calibration beam as summarized in Table 3.5.

Since magnetic dipole setting of the BIGRIPS spectrometer define the energy of each particle type we can calculate the expected momenta of each particle species measured. Small corrections to the momenta were propagated using LISE++ software which can calculate the energy loss through several materials in the beam line. These corrections resulted in a small change in the momenta. The measured momenta of the calibration beam differed significantly from the expected values as seen in Tables tables 3.1 to 3.3. This effect is attributed to inhomogeneities in the magnetic field which introduces electron drift velocity in the direction of  $\vec{E} \times \vec{B}$  direction. The  $\vec{E} \times \vec{B}$  drift velocity causes the electron trajectories to shift toward the +x-axis in the TPC coordinates causing particles of positive charge (going in the -x-axis) to have a higher measured momenta than in reality. The disagreement in measured and expected momenta is upwards of 5% difference in the

Momentum Resolution %	$\langle dE/dx \rangle$ Resolution %
1.6	4.6

Table 3.5: Summary of expected cocktail.

higher momentum calibration settings. The details of the correction technique are discussed in the later Section 3.2.6 are discussed in a more general correction which also includes correction for the space charge; the same correction technique was applied here in the special case of zero space charge which is the special case of only having  $\vec{E} \times \vec{B}$  components .

The values under the corrected column of seen in Tables tables 3.1 to 3.3, represent the data correcting for  $\vec{E} \times \vec{B}$ . A significant improvement is seen in the high momentum setting going from around 5% disagreement to within 1% agreement in the corrected data. For the lower momentum settings (Tables tables 3.1 and 3.2), protons see a slight improvement of about 1% where as the deuterons are over corrected in both settings. The level of agreement of the all corrected values is still within the estimated momentum resolution of the TPC.

Picture of cocktail before and after ExB effect Table of LISE++ expected cocktail energies  
ridigity setting of dipole magnets (reference big rips line)

### 3.2.2 Electronics calibration

The channel number of the electronics was calibrated by measuring the response of each channel to an input pulse supplied by a pulse generator. The pulse was injected into the ground plane of the TPC. This distributed the pulse evenly across the entire pad plane over a range of input voltages. The input voltage is plotted as a function of the measured ADC channel in Fig. 3.3 for every channel. The small variation in each channel can be seen as the wide band around each measurement point. A linear fit is performed to get the best fit line which provides a reference line which each channel is calibrated to. The right panel shows the resulting distribution of channels after calibration. This is a relative calibration technique meant to calibrate the varying gains in each channel relative to one another.

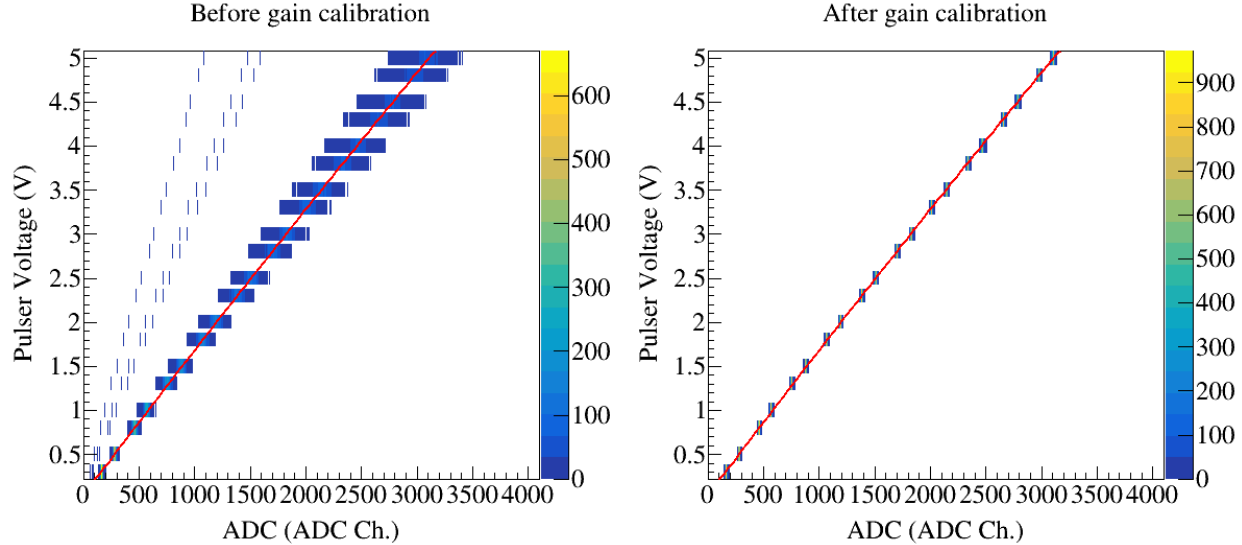


Figure 3.3: Calibration of electronics

### 3.2.3 Anode gain calibration

As mentioned earlier, the anode wires were separated into 14 independently biased sections. The high voltage of sections 12 and 14 were reduced during the experiment due to high currents being observed on the wires. The wire section voltages were lowered once and adjusted once again. Out of all the runs used in the analysis in this thesis .1, the anode sections 12 and 14 were lowered to 1085 V for runs 2272-2371 and set to 1214 V for all the other runs. By lowering the voltage on these anode wires, the gas gain is lowered as compared with all the other anode wire plane sections which operate at 1460 V. To account for the drop in gain, in the software we increase the gain of the pads which lie above these anode wires. To calibrate these sections we perform a relative calibration to the high gain anode sections by comparing the energy loss values of the high and low gain sections.

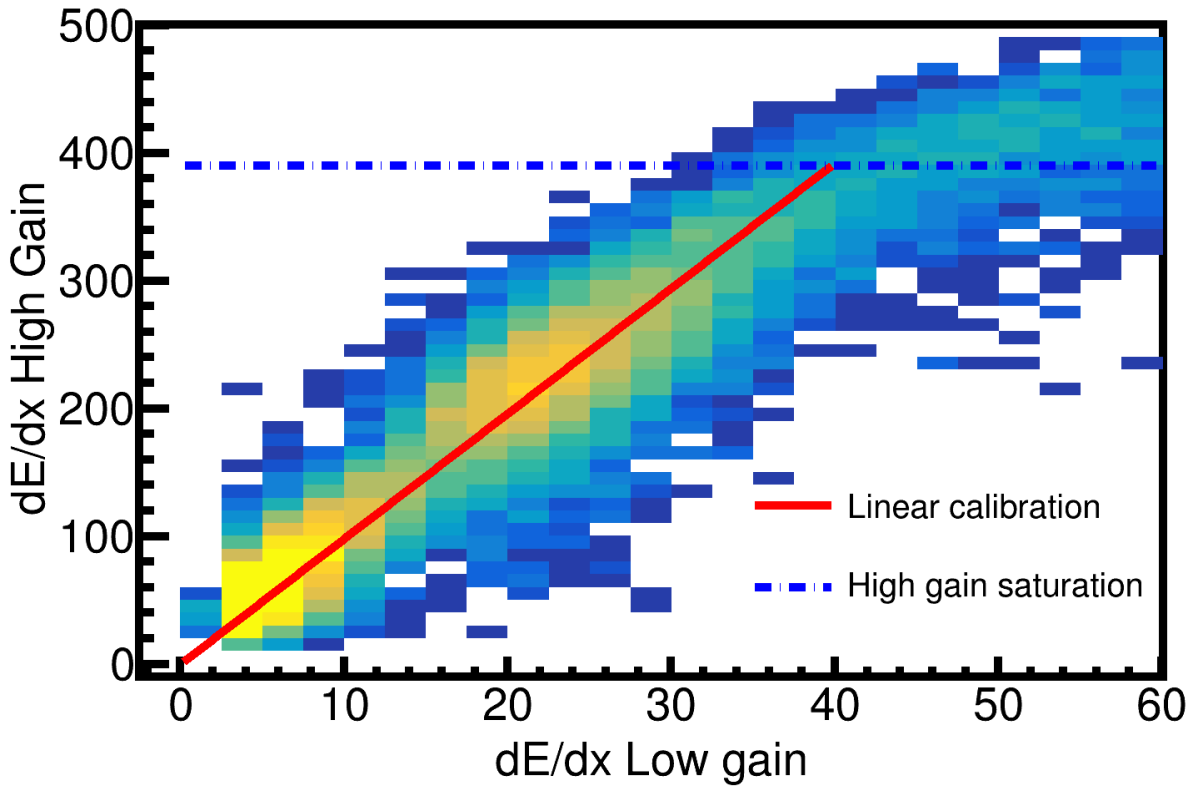


Figure 3.4: Calibration of low high.

### 3.2.4 Extending the dynamic range of the Electronics

Using a TPC for measurements of HIC in nuclear physics presents a different set of challenges as opposed to higher energy experiments. Typically in higher energy experiments the charge of particles is  $Ze$ , where  $Z=1$ . Also the particles are traveling at higher energies in which the energy losses in a detector range from the minimum of the energy loss curve to the small logarithmic climb CITE FIGURE HERE!!!. The dynamic range of electronics in such experiments can cover a wide range of particle energies in the energy loss curve. In nuclear HICs, we are interested in cluster of nucleons typically from  $Z=1-3$  resulting from the collision, and even higher in some applications. As seen in Eq. 2.1, the energy loss is proportional to  $Z^2$ ; the energy values of the resulting particles are at much lower energies which are in the  $1/\beta^2$  region. The energy range and particle types covered by the electronics are significantly limited as they quickly reach the dynamic

range limitations of the electronics as the charge of a particle increases and the velocity decreases.

Several TPCs have tried to address this issue by having regions of low and high gain, either in amplification gain or in electronics gain. Here we run into the issue that high velocity particles will have little to no signal in the low gain regions. At lower velocities, particles will deposit much charge over the low gain regions but will saturate the high gain regions, whose charge values are usually lost. Only within the dynamic range will tracks have the best momentum resolution, outside the dynamic range clusters will be missing in the sections which depend on the track velocity, lowering the momentum resolution of tracking. There are ongoing efforts in the nuclear community to develop new electronics which hope to mitigate these persistent issues in TPC electronics CITE HERE, by being able to switch to a lower gain value when the maximum range is reached. Though, it is quite useful to develop a software technique which may extend the dynamic range of TPC electronics without the use of external hardware, especially in experiments which have already been performed with older electronics technologies.

In TPCs, the effective dynamic range can be very different from the single pad dynamic range. Typically TPCs are operated inside of a magnetic field for reconstructing momentum of each particle, which requires sub-millimeter precision in the position determination of the track path. This is achieved by averaging the charge distribution over several pads which is discussed in Section CITE HERE. Therefore the effective dynamic range is related to the relative charge values of adjacent pads (between the center pad and outside pads). For example, to measure minimum ionizing particles the signal to noise ratio of the pad with the smallest charge in the distribution should be some reasonable value, say at least 6:1. From Section CITE HERE we know the central pad in the cluster holds 80% of the total charge, whereas the two adjacent pads each hold the remaining 10%. If we require the adjacent pads to have a signal-to-noise ratio of 6:1, then the central pad would have a signal to noise ratio of 50:1. Considering this is the signal-to-noise ratio for minimum ionizing particles, and the maximum signal-to-noise ratio is 800:1, this means the effective dynamic range in the TPC is roughly 16 times that of minimum ionizing particles. The dashed lines and vertical blue bar in Fig. 3.5 are separated by a factor of 20, representing the typical

effective dynamic range in a TPC. This dynamic range estimate should be regarded as approximate because the energy loss fluctuates significantly about the most probable energy loss, with a long “Landau” like tail, as described by Bichsel [?]. Nevertheless, the blue dashed lines and vertical blue bar illustrate that the range of energy losses sampled in a fixed gain readout system is limited. One can change the gain and shift the energy loss range that can be sampled, but the dynamic range itself cannot be increased.

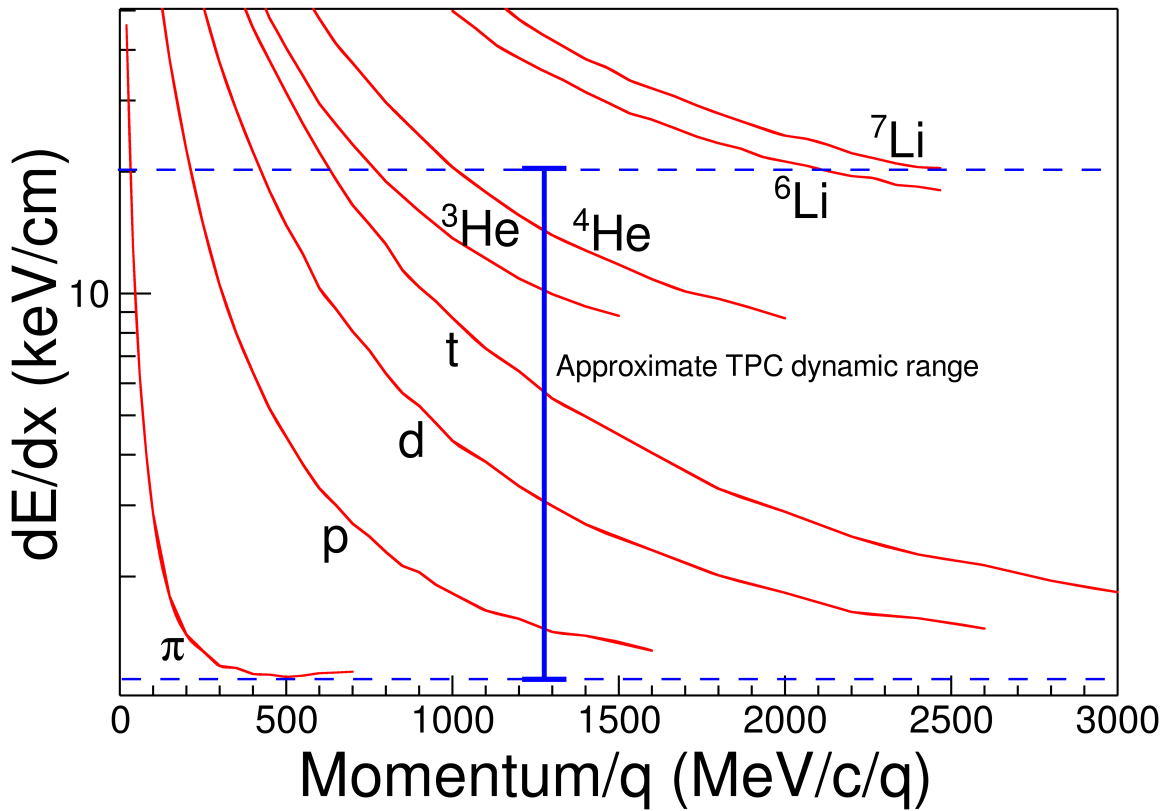


Figure 3.5: The expected  $dE/dx$  lines of different particles are given in red as calculated by Geant4. The approximate dynamic range of the TPC is shown by the vertical bar for the gain setting used in the experiment. Anything outside of this region would be saturated to some degree.

The rapid increase in the stopping powers at low momentum illustrates the degree to which the effective dynamic range can be exceeded and highlights the problems encountered in studies of intermediate HICs, in which light particles with low momenta are abundantly produced along with highly charged particles. Similar problems are encountered when TPCs are used as active targets in direct reaction studies with rare isotope beams [?].

Several techniques have been employed to increase the observable range of energy losses. This can be done by lowering the electronics gain of selected readout channels, or by changing the gas amplification at the readout plane in certain areas of the TPC. In the EOS TPC [9] this was done by decreasing the voltages in select anode wires in the multi-wire readout. With the prototype Active Target TPC lowering or increasing the gain was achieved by decreasing or increasing the electric fields on selected pads within a Micromegas [?]. The results of changing the gas-gain, or the electronics gain, are rather similar in that reducing the gain to sample a range of higher energy loss makes the TPC effectively blind to minimum ionizing particles in the regions of lower gain.

We define the clustering direction depending on the angle of the track, at the point of each cluster, with respects to the  $x$  axis, defined as  $\theta$ . For example, the crossing angle is defined as  $90^\circ$  for a track going along the  $z$  axis, and  $0^\circ$  for a track going along the  $x$  axis. In the case that the crossing angle is  $45^\circ < \theta \leq 90^\circ$  the clustering direction is along the  $x$  axis. For  $0^\circ < \theta \leq 45^\circ$  it is along the  $z$  axis.

The position along the clustering direction is calculated by weighting the individual hit's positions by their charges  $q_i$  and getting the mean value. The other direction is set to the center of the pad. For example, if we are clustering along the  $x$  axis for a cluster, the  $z$ -position is set to the center of the pad in the  $z$ -direction and vice versa.

### 3.2.5 Method of Desaturation

We will use the term “desaturation” for our process of correcting the charge values of the saturated pads. Figure 3.7 shows a typical situation of saturated signals. When an avalanche causes a large induced signal, the pads directly underneath collect the largest charge becoming saturated, denoted as  $q_2'$  and  $q_3'$ . Pads further away experience smaller, non saturating charges, denoted as  $q_1$  and  $q_4$ . Though we do not know the saturated charge values, the distribution of all charges must follow the PRF which we have experimentally measured. From the clusters crossing angle, we can get the corresponding parameters for the PRF as described above and in Fig. 2.3.

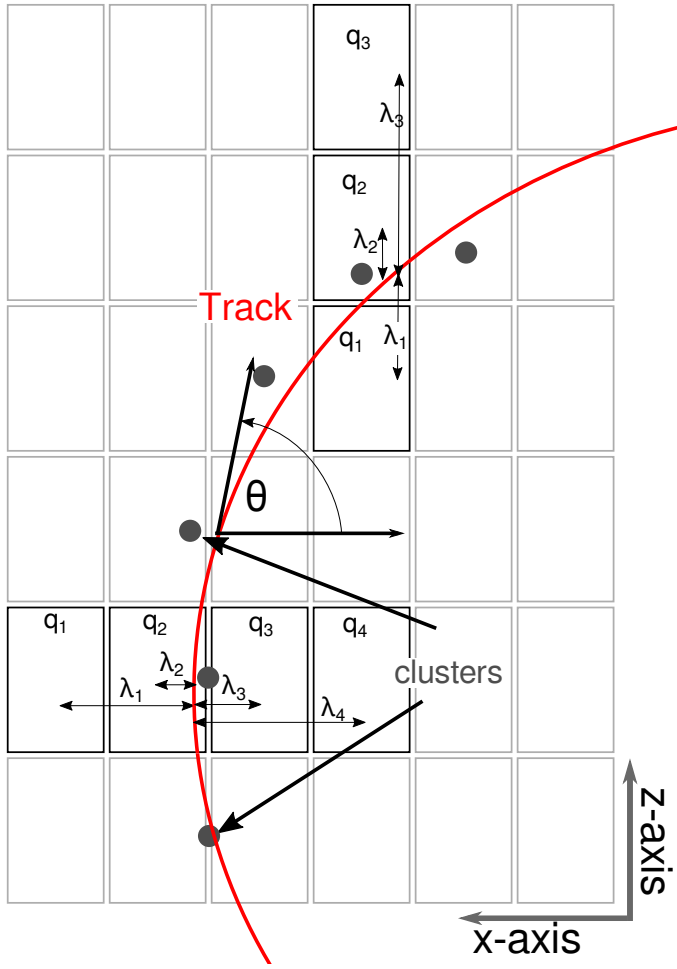


Figure 3.6: Cartoon of a top down view of a fit to a track passing through several pads. The bolded pads and the charges  $q_i$  represent the hits belonging to that pad and the clusters of the track representing the average position of the track. The three clusters at the bottom are clustered in the  $x$ -direction for the upper three are clustered in the  $z$ -direction. The estimated position of the avalanche is given by the track fit, and the position from the center to each pad to the  $\bar{x}$  position is given as  $\lambda_i$ .

We assume the distance of each pad to the track,  $\lambda_i$ , is fixed, defining the fraction of charge each pad receives as given by the  $PRF(\lambda_i)$  function.

$$\chi^2 = \sum_i \frac{(q_i^{\text{obs}} - q_i^{\text{expect}})^2}{q_i^{\text{expect}}} \quad (3.1)$$

To determine the best estimate for the charge values of each saturated pad, a chi squared function is minimized, given in Equation 3.1, where  $q_i^{\text{obs}}$  are the observed, non-saturated charges  $q_1$  and

$q_4$ , and  $q_i^{\text{expect}}$  are the charges we expect to observe, calculated as  $q_i^{\text{expected}} = Q \cdot PRF(\lambda_i)$ . The charges  $q_{2'}$  and  $q_{3'}$ , make up the unknown variable and are allowed to vary in the  $\chi^2$  minimization, where they are added to make up the total expected charge  $Q$ .

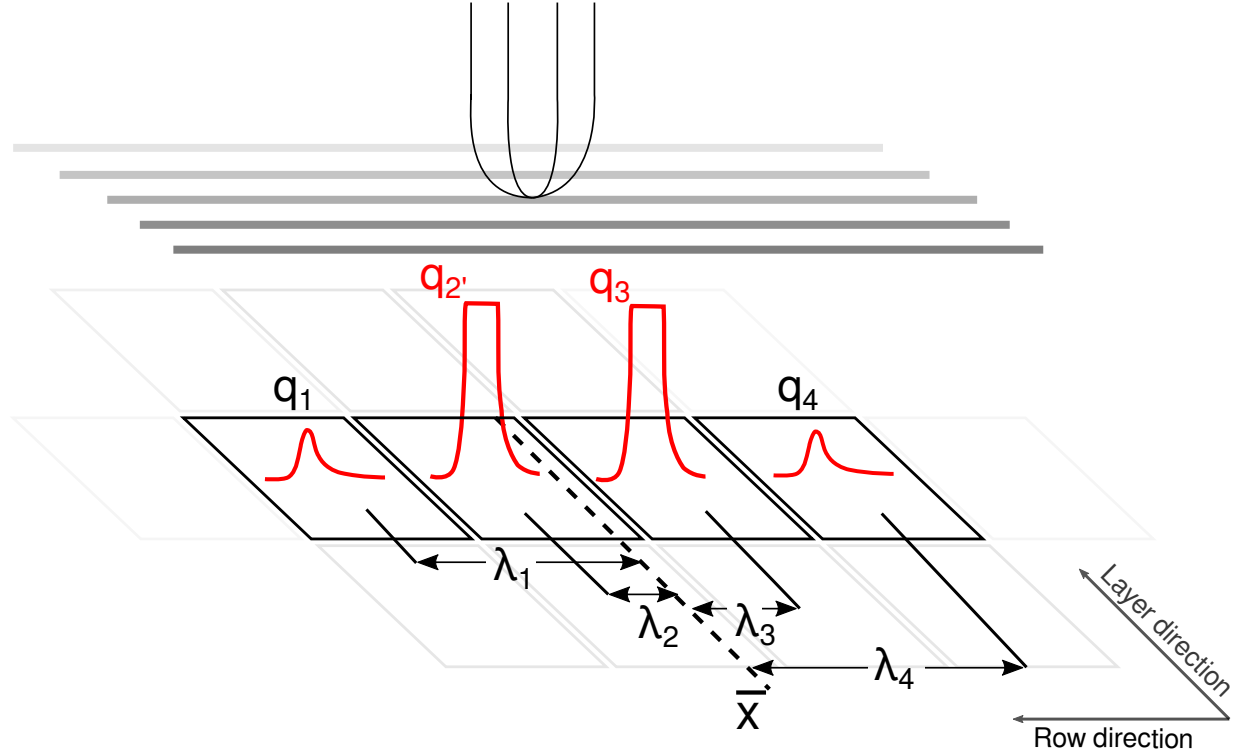


Figure 3.7: A typical case of a saturating event. The red pulses represent the time bucket signal for each collected charge. The pads directly underneath the avalanche point,  $q_{2'}$  and  $q_{3'}$ , are saturated while pads farther away,  $q_1$  and  $q_4$  are not saturated.

Shown in Fig. 3.8 is a typical cocktail event, where one particle enters the TPC volume at a time and parallel to the pad plane, representing an ideal case for momentum and  $dE/dx$  determination; as it does not suffer from inefficiencies of high multiplicity events seen in the collision experimental data.

Tracks which saturate pads in the high gain region are not saturated in the low gain region. By comparing the  $dE/dx$  values of these two sections, we can directly measure the success of the desaturation in the high gain regions using the method described above.

In Fig. 3.10, the effect of saturation can be seen in the high gain region for the uncorrected

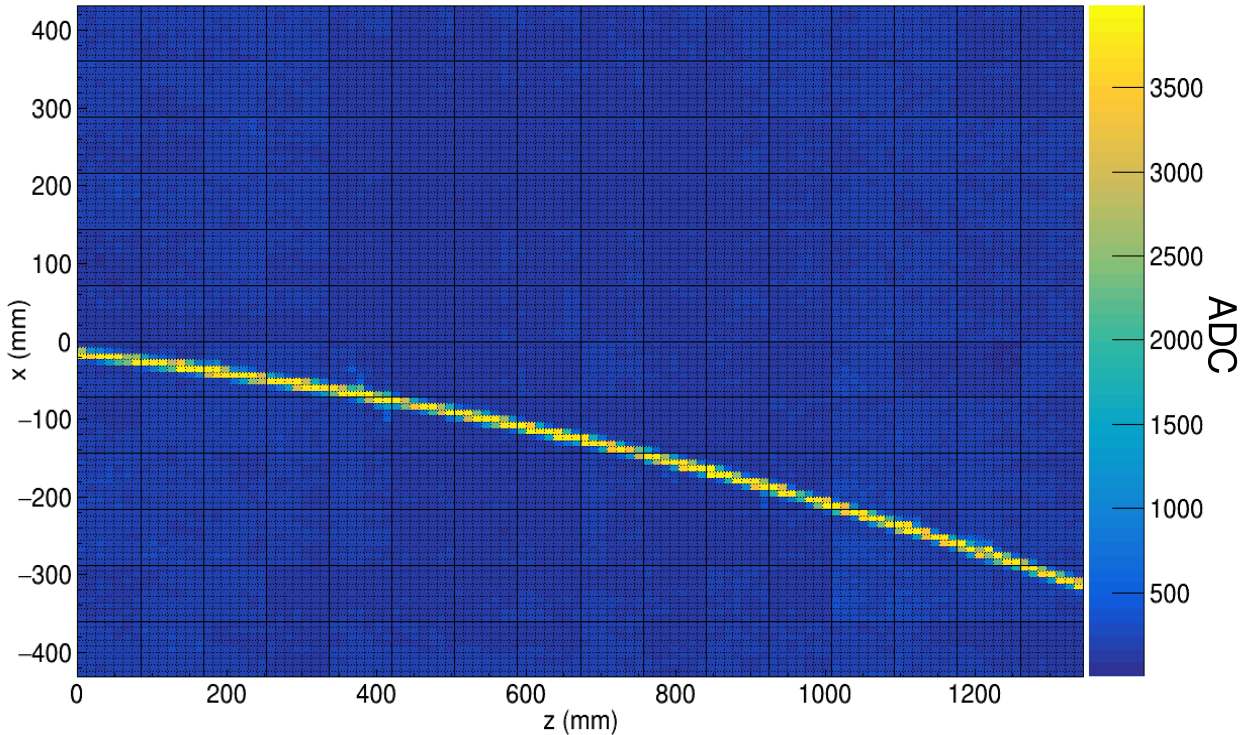


Figure 3.8: Pad plane projection for a cocktail event in the TPC.

data. For signals below  $400 \text{ ADC/mm}^1$  the electronics are not saturated, and therefore the high and low gain sections agree. The data starts to saturate above  $400 \text{ ADC/mm}$  in the high gain channels eventually reaching a plateau while the low gain sections are not saturated and provide the true  $dE/dx$  values. After applying the desaturation method, the correlation between the high and low gain sections is restored, as seen in Fig. 3.10. From this comparison, we infer that the correction works up to signals of  $2000 \text{ ADC/mm}$ , increasing the dynamic range by a factor of at least 5.

Comparing the low to high gain sections directly validates the desaturation technique, but the goal of this exercise is to improve the particle identification (PID). In the following PID plots the red lines represent the most probable energy loss as given by Geant4 straggling functions. A linear calibration was performed to convert keV in Geant4 to ADC in the experiment given by  $\text{ADC}/\text{mm} = 19 \text{ keV/cm}$ .

There are pronounced PID lines of several particle species in both the uncorrected and corrected

---

<sup>1</sup>Un-calibrated ADC channels in arbitrary units.

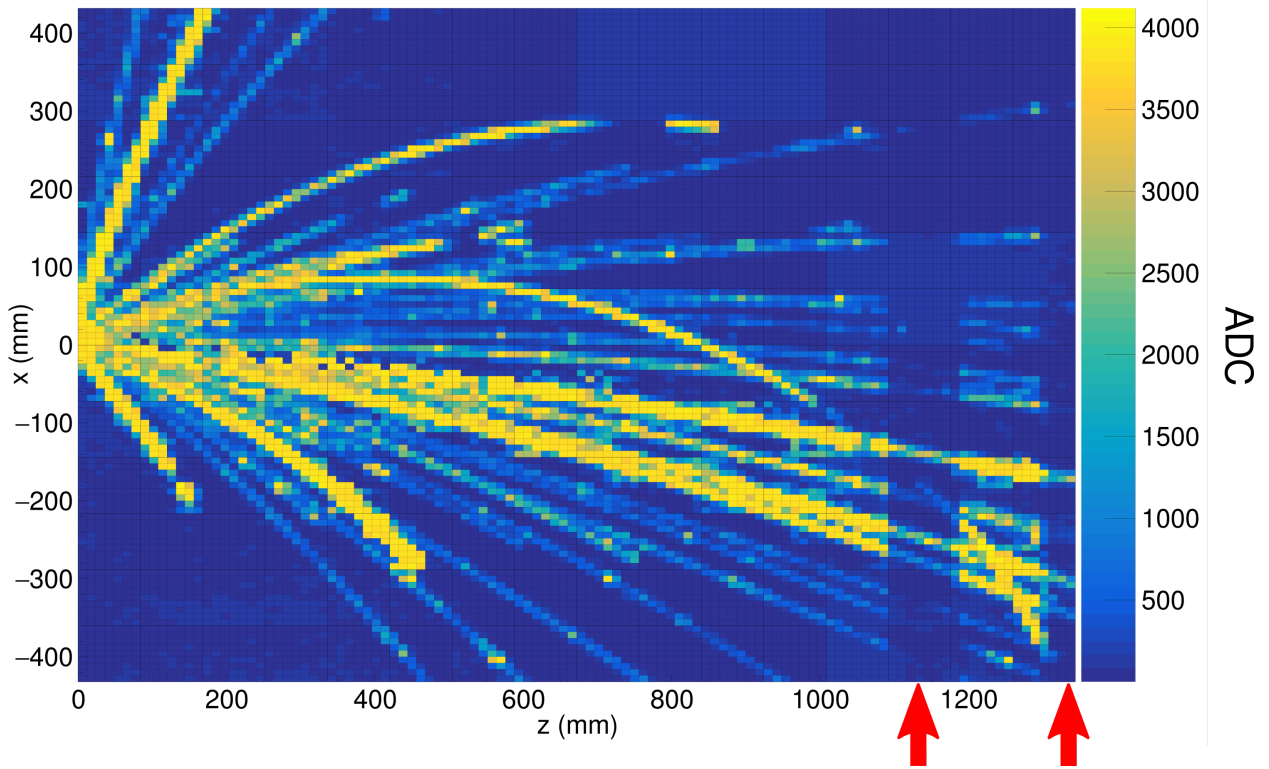


Figure 3.9: Pad plane projection for a collision event in the TPC. Highlighted by red arrows are two regions of anode wires which had a reduced voltage of 1214 V. The voltage of the rest of the TPC anode wires are 1460 V. The reduction in voltage reduces the gain by a factor of about 10.

cocktail beam PID shown in the subplots of Fig. 3.11. Three ovals around a momentum of 1700 MeV/ $c/q$  and two near 900 MeV/ $c/q$  correspond to the three  $B\rho$  settings injected into the TPC. The tails of the PID lines are resulting from the particles passing through the walls and other materials outside the main detector volume, therefore lowering the initial momentum.

The uncorrected data in Fig. 3.11 shows the effects of saturation; the PID lines deviate from their theoretical expectations starting at around 400 ADC/mm eventually reaching a plateau. After applying the desaturation technique, we see a large improvement, most notably for the He and Li particles, which suffer the most from saturation. A more subtle improvement of the lighter particles, ( $p, d, t$ ), can also be seen in the PID lines at lower momenta.

Looking at the collision data, shown in Fig. 3.12, we also see a similar result. In the collision data, the PID suffers from more background and inefficiencies than the cocktail beam, nevertheless we can see a similar improvement in the PID lines when comparing before and after applying

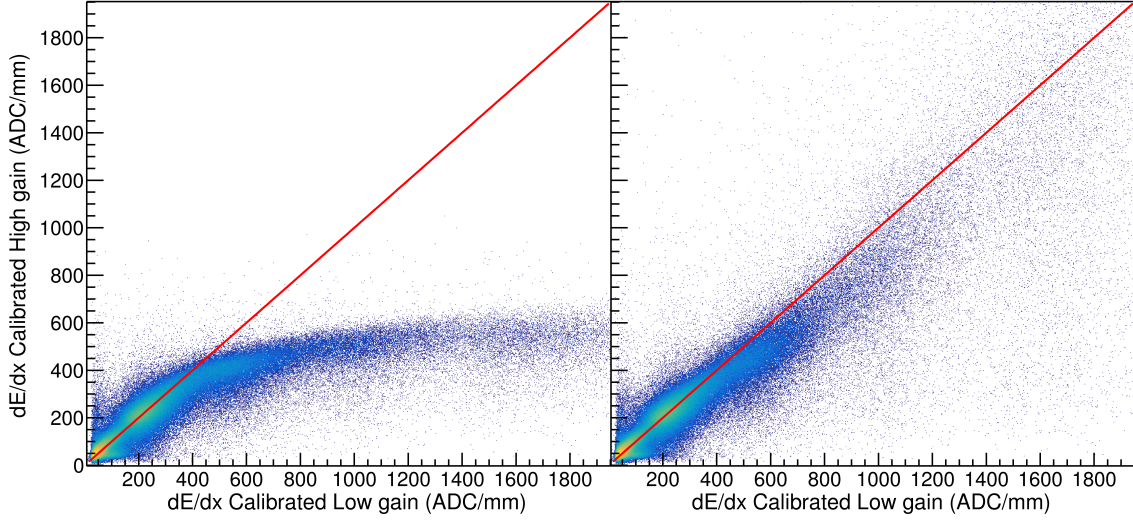


Figure 3.10: The left panel shows the high gain stopping power vs low gain when the method of desaturation was not applied. In the right panel the desaturation technique was applied to the high gain region. The low gain does not suffer from saturation and represents the true  $dE/dx$  value.

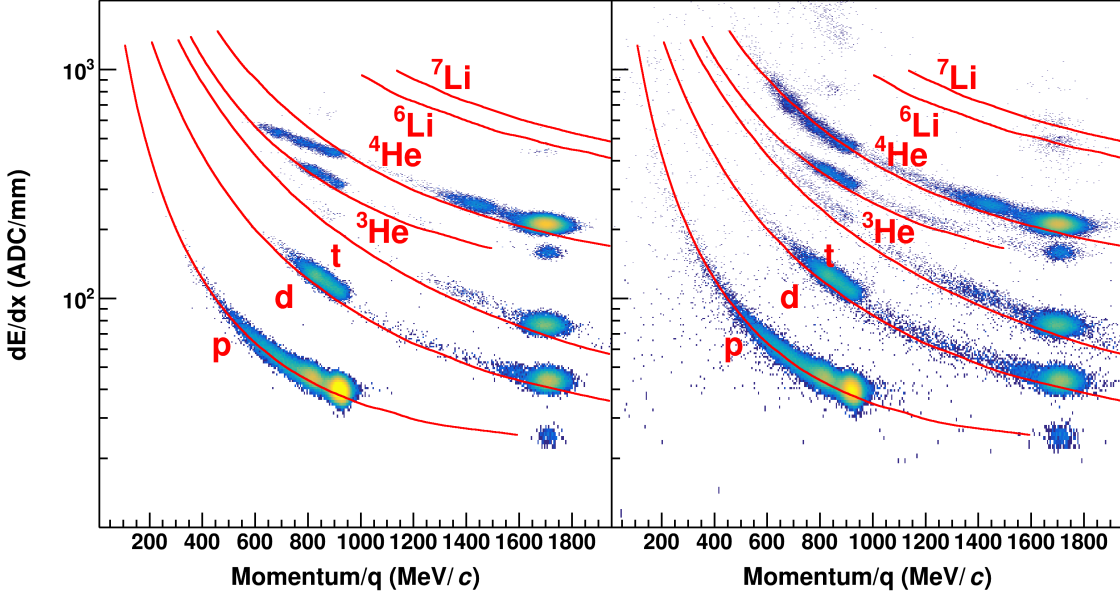


Figure 3.11: Uncorrected (left panel) and desaturated (right panel) cocktail data.

desaturation. Notably the largest improvement is the separation of particle species at lower momenta and the separation of the Li species into  ${}^6\text{Li}$  and  ${}^7\text{Li}$ . In these regions, there was little to no PID resolution before desaturation.

The dynamic range was extended by at least a factor of 5, as demonstrated by the improved PID

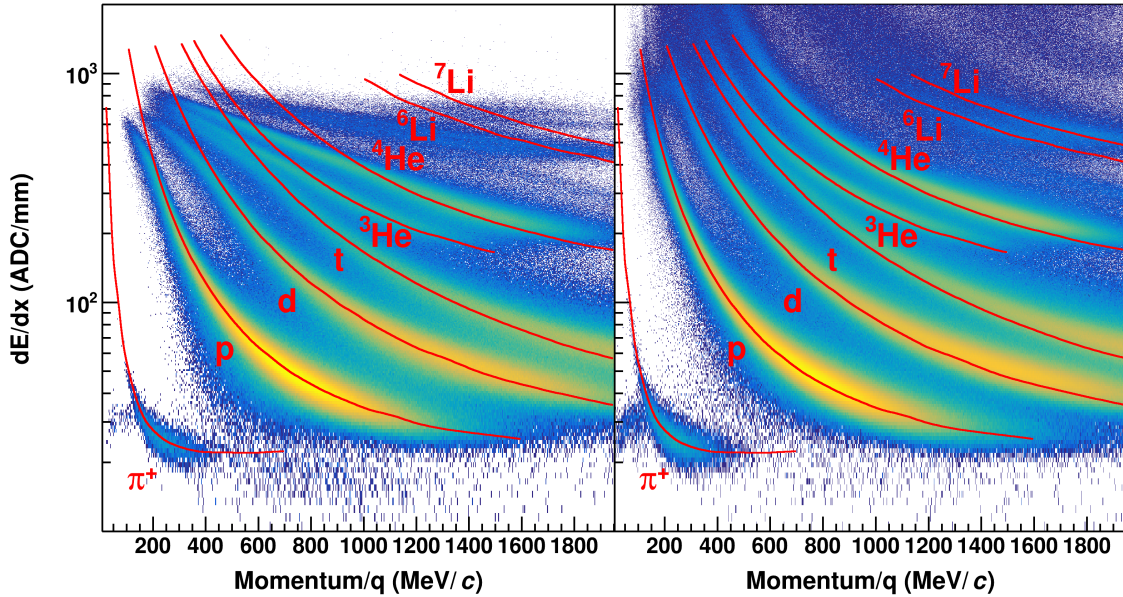


Figure 3.12: Uncorrected (left panel) and desaturated (right panel) collision data at polar angles of  $\theta < 40^\circ$  and azimuthal angles between  $-80^\circ < \phi < 80^\circ$

lines, and quantified by direct comparison to low gain sections of the TPC. This improved PID will allow for us to extend the momentum distributions of all species to lower momenta and to heavier ions than what was previously available.

### 3.2.6 Space Charge Corrections

MAYBE ADD A LITTLE NAPKIN CALCULATION OF SPACE CHARGE TO SHOW ORDER OF EFFECT.

Beam Energy Loss	$^{132}\text{Sn}$	$^{124}\text{Sn}$	$^{112}\text{Sn}$	$^{108}\text{Sn}$	Avg.
keV cm $^{-1}$	11.2	0.034	5.43	903	150

Table 3.6: Average energy loss of each beam.

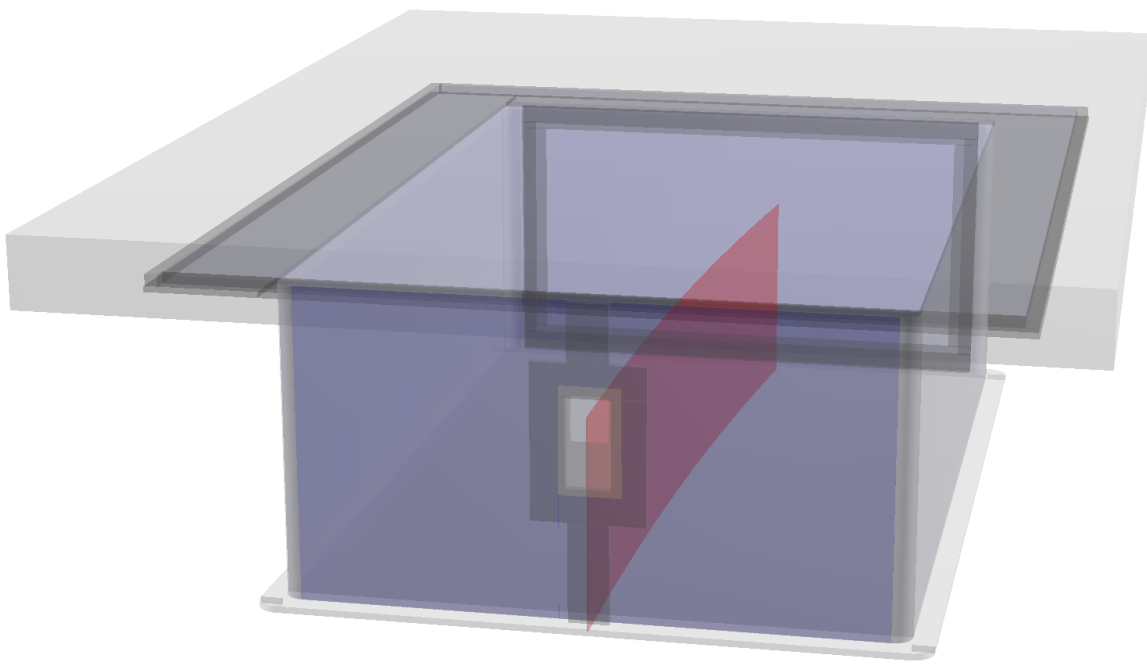


Figure 3.13: Location of space charge in  $^{132}\text{Sn}$

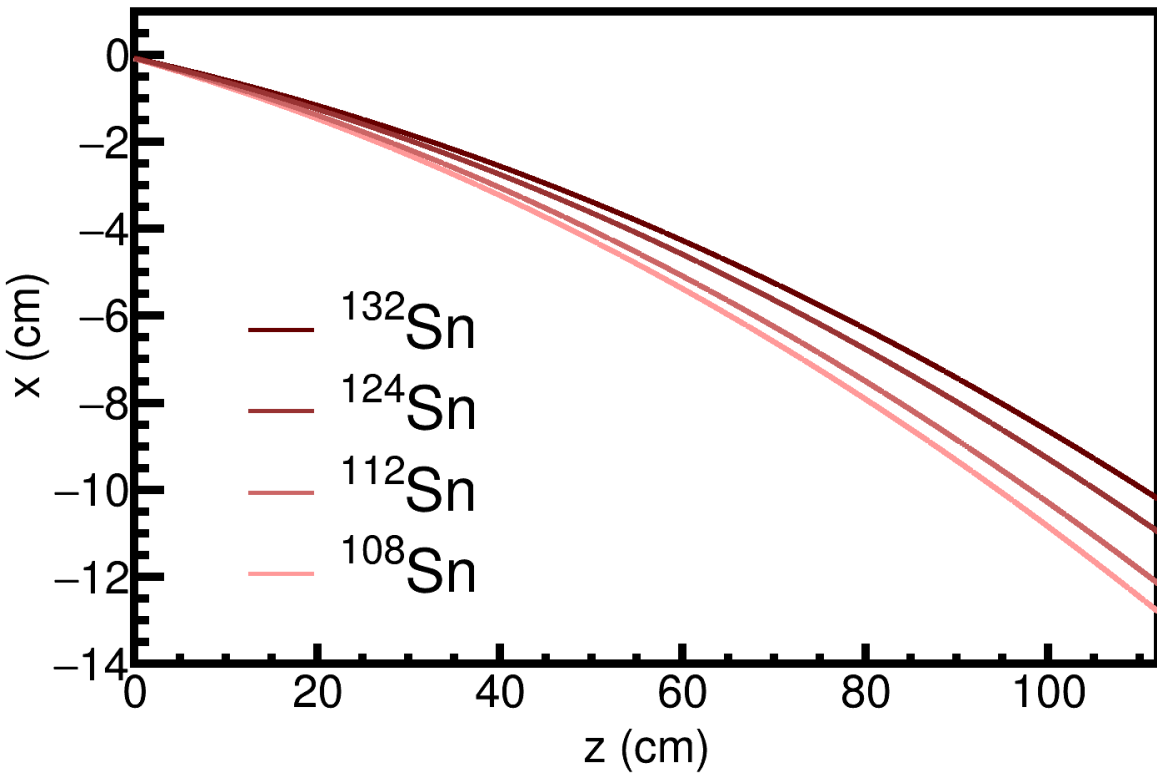


Figure 3.14: Beam path of the experiments

As the beam passes through the field cage it ionizes the gas along the way creating electron-ion pairs. The drift velocities of the ions are  $1 \times 10^4$  times slower than the electron drift velocities. Because ions move very slow, the potential build up of positive ions may create a space charge which distorts the drifting electrons of the tracks, impacting the measurement of their momentum. There are several regions of the TPC in which electron-ion pairs are created. The largest source of positive ions are created in the avalanche process near the anode wires. These ions slowly drift toward the cathode and are captured by the gating grid. The other source of ions come from the primary ionization produced by the beam and reaction products in the detector gas. The energy loss  $\langle dE/dx \rangle \propto Z^2$ , where  $Z$  is the charge of the particle type. Because the charge of the un-reacted beam is around  $Z \approx 50$ , the ionization due to the beam is a factor of  $2.5 \times 10^3$  times that of the light charged particles which mostly are of charge  $Z = 1$ . The beam is positioned about 25cm below the anode plane in the TPC. It takes electrons approximately 5 $\mu$  sec to drift to the anode plane. It takes

the ions  $5 \times 10^4 \mu\text{sec}$  to travel. The beam rate in the experiment varied around a value of about 10kHz, which has an average occurrence of 1 beam every  $100\mu\text{sec}$ , which is much shorter than the time it takes for the ions created by each beam to terminate on the cathode plane. This results in a build up of positive ions in the shape of a sheet charge, carved out by the beam path as shown in Fig. 3.15. The average distance between sequential ion paths created by each beam is a spacing of about  $50\mu\text{m}$  apart, and the average number of beam paths that compose the sheet charge is around 500 tracks. Though the arrival time of each beam track is random, the large number of tracks, and small inter beam spacing, allows us to approximate the sheet charge as an uniform sheet charge.

The electric field in the presence of the sheet charge can be calculated by solving Poisson's equation,

$$\nabla^2 \phi = \rho, \quad (3.2)$$

where  $\phi$  is the electric potential and  $\rho$  is the free space charge; given the Dirichlet boundary conditions of the field cage. The electric field is given as the gradient of the potential,  $\vec{E} = -\nabla\phi$ .

To reduce computation time, we notice that  $\vec{E} \propto \rho$ , we can therefore solve the electric field for a reference free charge  $\rho_0$  and scale the solution for any other free charge. The full magnetic field map is provided by the SAMURAI collaboration [10]. The velocity field map is given by Eq. 2.5 and the electron drift through this velocity map is propagated by using a time stepped 4<sup>th</sup>-Order Runge-Kutta integration. The correction map is calculated by starting from the anode y-position and the measured (x,z) on the pad-plane and stepping backward in time in the Runge-Kutta integration through the velocity field map until the electron reaches the measured y-position.

It has been shown before that the amount of space charge present in the chamber is related to observables such as the distance of closest approach of each track to the vertex point [11]. This is easily understood, as the space charge distorts the electrons as they drift through the chamber eventually distorting the overall shape of the measured track. In the presence of no space charge, you would correctly expect the distance of closest approach of each track to the vertex point would

be a distribution centered around zero. In the presence of space charge the tracks are distorted and the distribution has some mean bias.

Shown in Fig. 3.18 is an example of the distortion map in the TPC for left-going tracks in blue, and right-going tracks in green, with the vectors of distortion magnified. The space charge affects left and right going tracks differently, with the right-going tracks going to higher momentum values and the left-going tracks going to lower momentum values. The inset figure of Fig. 3.18 shows the shift in the x-position distance to vertex for the displaced left-going track given by  $\Delta V_x$ , with the opposite direction for right-going tracks. We are able to measure the amount of distortion the space charge creates by measuring the difference between the most probable values of the left-going and right-going tracks which we define as  $\Delta V_{LR}$ .

Overview Discuss the relevant time scales, drift lengths, magnitudes, and locations of space charge

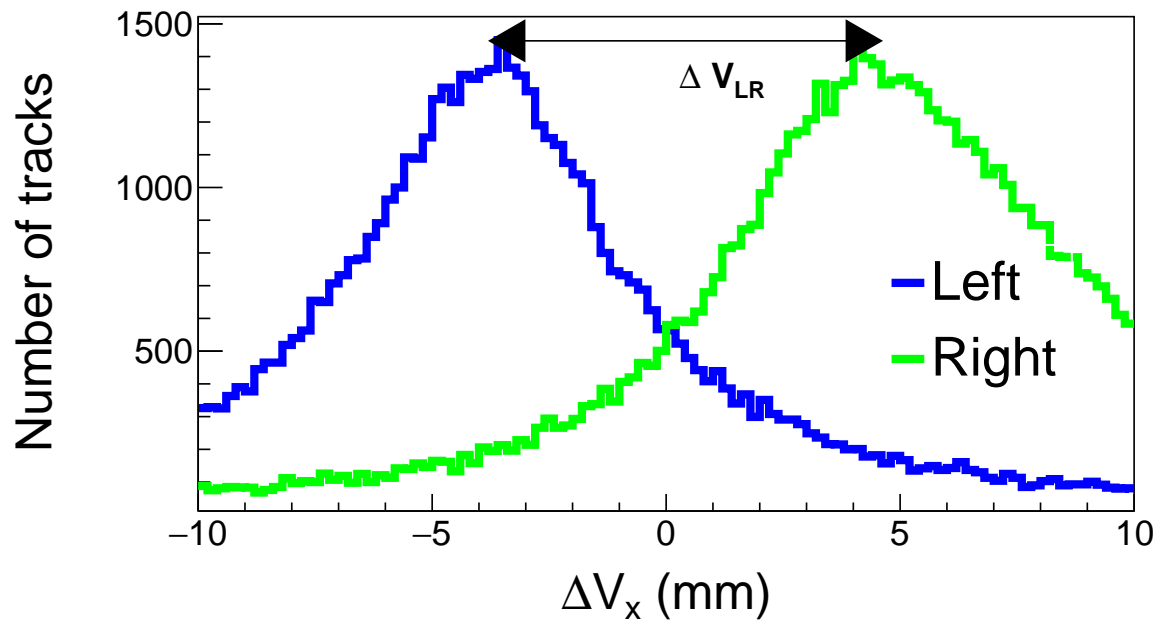


Figure 3.15:  $\Delta V_x$  distribution for left-going and right-going tracks in the TPC for the

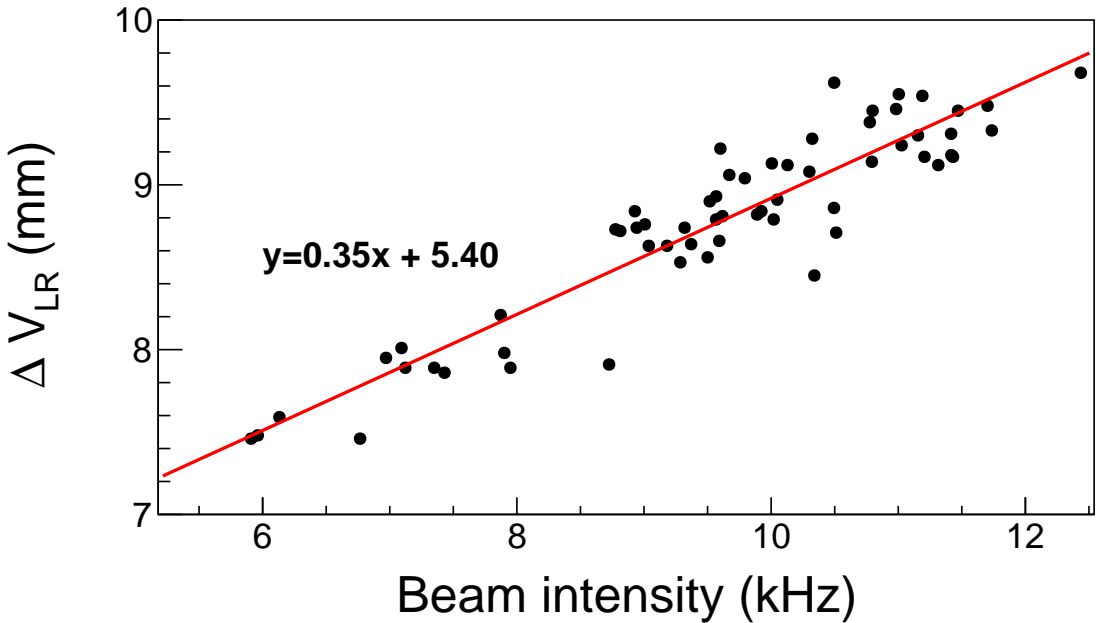


Figure 3.16:  $\Delta V_{LR}$  as a function of the beam rate.

The average beam rate was recorded in each experimental run and slightly varied from run to run, due to beam production variations. The amount of space charge present in the field cage is directly proportional to the beam rate; therefore  $\Delta V_{LR}$  is also proportional to the beam rate as shown in Fig. 3.16. The only parameter in the space charge correction algorithm is the surface charge density  $\sigma_{SC}$ . By varying  $\sigma_{SC}$  for a wide range of values the  $\Delta V_{LR}$  observable is measured and plotted in the left panel of Fig. 3.17. The surface charge density which gives  $\Delta V_{LR} = 0$  is taken to be the estimate for the average amount of space charge present. This is done for several runs which vary in beam intensity. Since the relation is linear between the surface charge density and the beam rate, a linear fit gives good agreement for interpolating the surface charge values as a function of beam rate, as seen in the right figure of Fig. 3.17.

This is done for all the systems. I NEED TO PUT THE ASSUMPTIONS of SPACE CHARGE SHEET DENSITY OF 132 108 HERE!!!

From the BDC tracking, the precise interaction point on target is known. Using this point

greatly improves the momentum resolution of the track fitting, but there is a systematic shift when comparing the momentum value without using the vertex BDC point in the fit. The space charge affects right-going and left-going tracks differently making right-going tracks more rigid (higher momentum) and left-going tracks less rigid (lower momentum). For polar angles of  $\theta < 40$  deg, the disagreement between momentum values fitted with the BDC, versus without, are much less because the projection of the track does not disagree as much with the BDC point as tracks with polar angles of  $\theta > 40$  deg. This is seen in

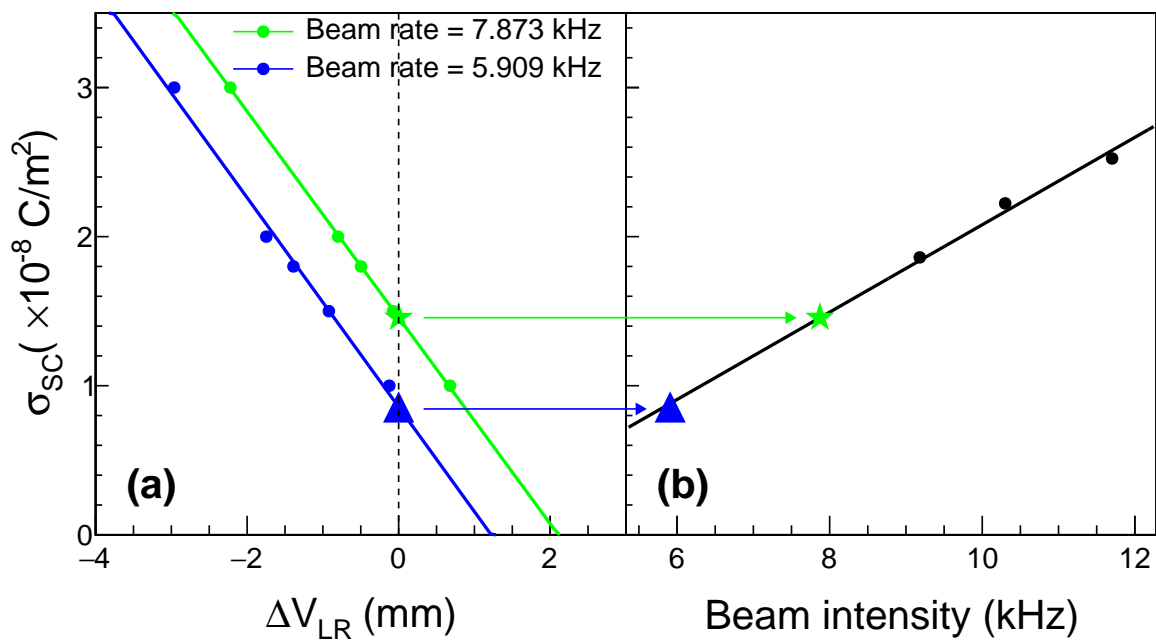


Figure 3.17: Space charge relation

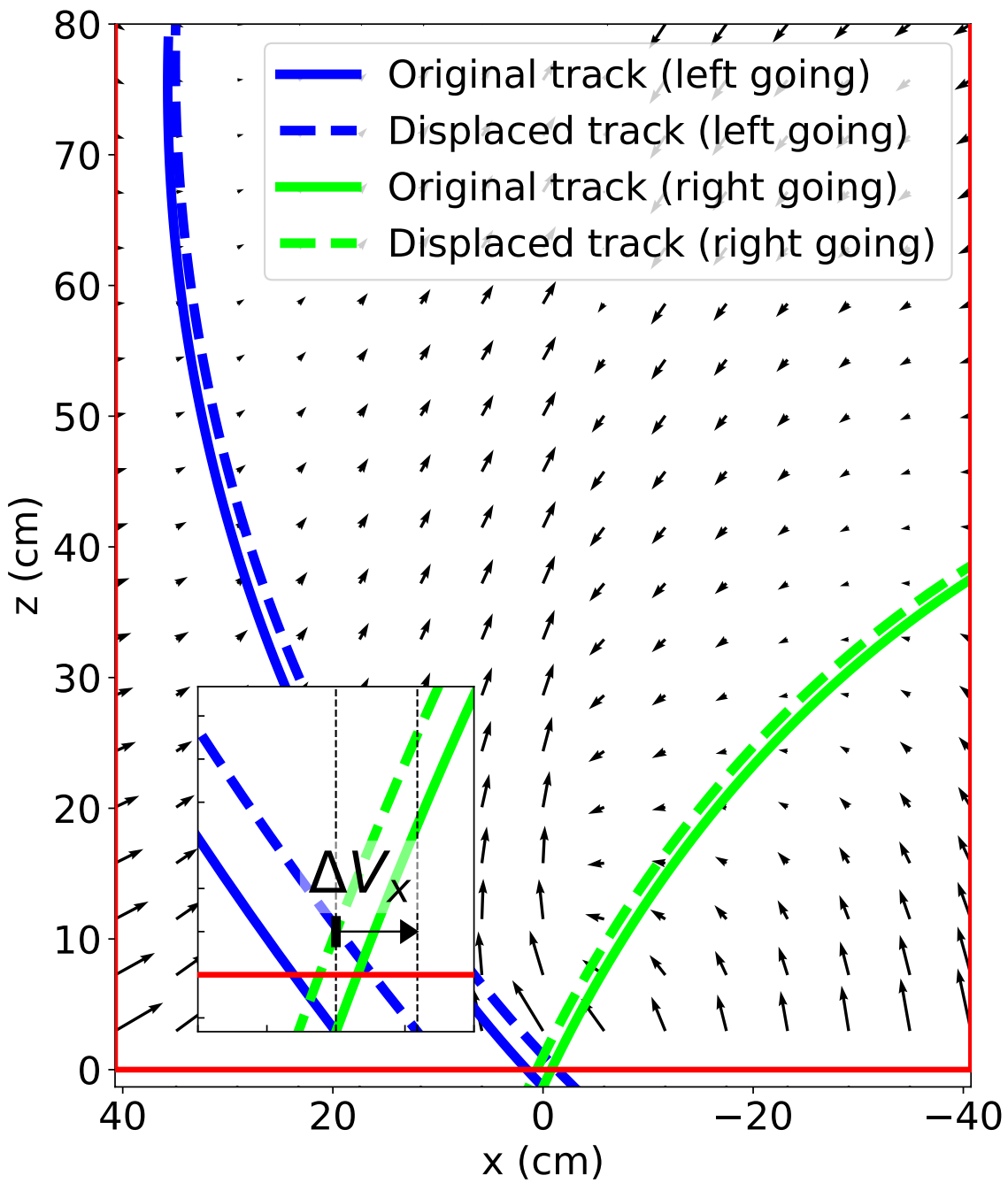
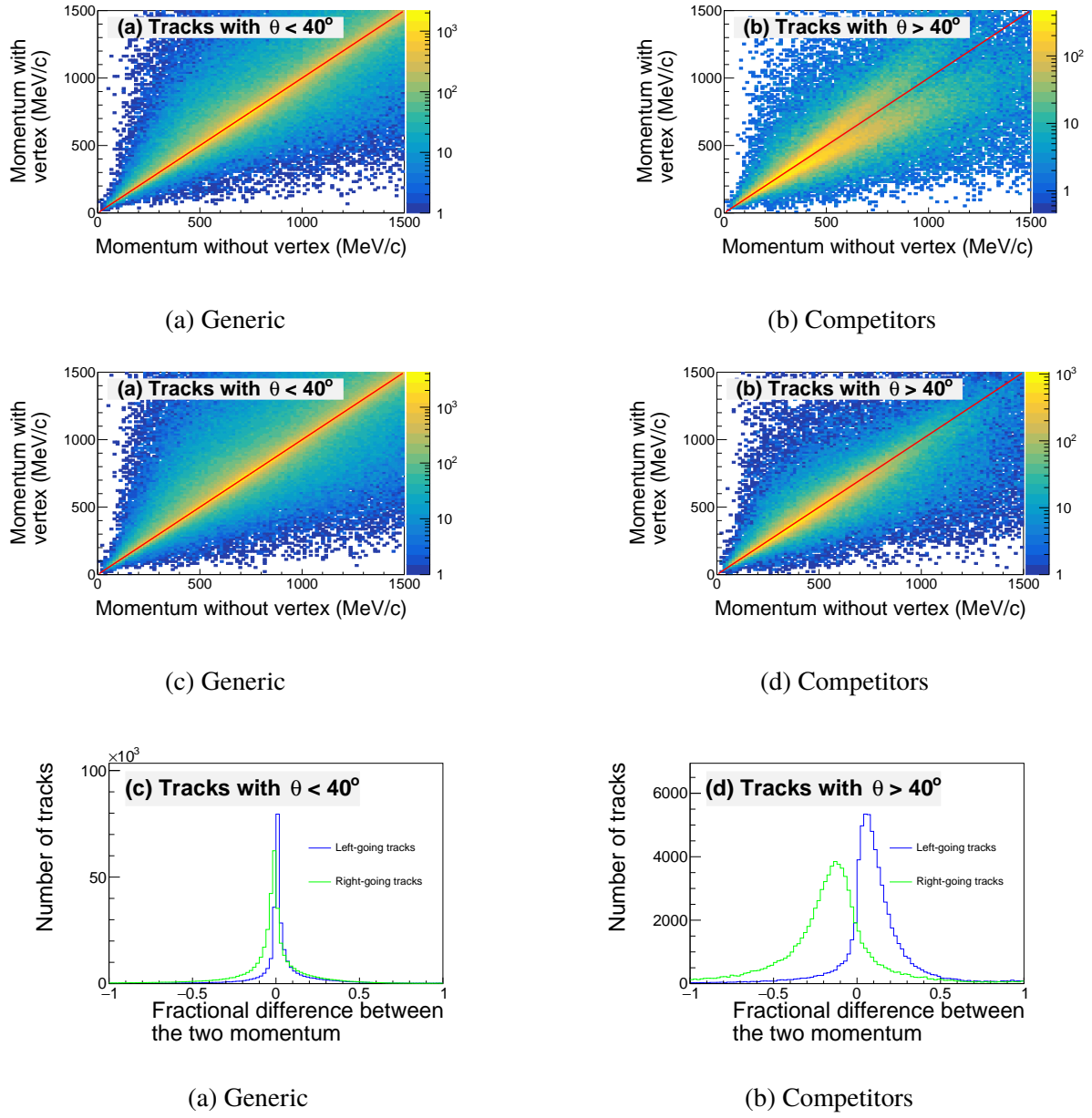


Figure 3.18: Shift of tracks



Reference appendix for poisson solver Tables for ion drift velocity in P-10 Gas reference Sauli

Figure of sDAC or POCA Figure of cartoon of what is happening to tracks Figure of correction map in TPC and MC map Figure of before and after correction BDC vs reco momentum Figure of track residuals before and after?

In theory, a TPC functions with the electric and magnetic fields parallel to each other. In this way the electrons move opposite to the electric field winding tightly around the magnetic field

lines, reducing transverse diffusion in the process. In practice, due to the finite size of the dipole magnet and field cage, there are traverse components to both the electric and magnetic fields. These transverse components introduce drift velocities in the transverse directions, causing a shift in the measured cluster positions of the track. Thereby introducing systematic shifts in the calculation of the momentum and the vertex calculation.

Most of the time the beam does not undergo a nuclear collision with the target and passes through the TPC drift volume. The KATANA array threshold was set to veto such events, ensuring the gating grid remain closed to prevent the large amount of charge deposited by the beam into the avalanche region. While the electron drift velocity is fast enough for the electrons produced by the unreacted beam to terminate on the closed gating grid, the drift velocities of the positive ions produced are of order  $10^{-4}$  times slower. At higher beam rates the positive charge is allowed to pile up producing a region of positive space charge, introducing perturbations to the nominal electric field.

Since the beam comes in along the z-axis, and the drift direction of the ions is in the -y direction, we can estimate the charge density as an uniform sheet charge. The surface charge density is related to the beam rate, ion drift length, ion drift velocity, and the energy loss of the beam. Though the incoming beam comes randomly, the slow drift velocity combined with the high beam rate makes the uniform approximation valid. Tracking or estimating the beam rate as a function of time with in a given run would provide a better estimate of the space charge. Or experimentally a laser system could be pulsed after each event (throughout the drift volume), giving the experimental correction map for the drift. While the potential for a laser system was implemented in the field cage design, a laser system ultimately was not developed for the S $\pi$ RIT tpc.

The beam rate within a run is roughly constant, therefore we can estimate the space charge and provide a first order correction for the space charge effect.

As mentioned in CHAPTER ???, the cocktail beam momentum was well known to within 1% as set by the BIGRips spectrometer. Also time of flight analysis of upstream and downstream scintilators also independently confirmed the beam rigidity setting. The expected momentum is

given in TABLE ??? as calculated by from the beam rigidity setting of the magnet (WHICH MAGNET). The measured momenta as determined by the TPC software (given in FIG TABLE ), shows a disagreement on the level of 5% too high. We noticed that if one only uses the first 90 layers (out of 112) of the TPC, the momenta is lower; one should expect the momentum to go higher as the track length is shorter (short tracks effectively are straight lines). In the cocktail beam there is no un-reacted beam causing any significant space charge. The magnetic field map of the SAMURAI magnet has been calculated by TOSCA simulation CITE ???, and several points have been verified experimentally with a hall probe to be within XXX %. We assume that the electric field (to first order) is uniform in the y-direction. Using Garfield++ CITE ???, we can model the transverse drift of the electrons in the presence of such fields.

A grid of electrons uniformly distributed in the TPC model space were drifted to the gating grid position. The final shifts in the x and z positions was measured.

### 3.3 Monte Carlo Simulation

We use Geant4 as and event generator for performing Monte Carlo Simulations in the TPC. A scale model of field cage, front window, front window frame, pad plane, and aluminum top plate are modeled. The correct materials are used as well as the field cage is modeled with P-10 gas at a density of ??. By using Geant4 we can also input the the magnetic field map of the SAMURAI dipole magnet (as calculated by the SAMURAI group via a TOSCA simulation). In this way any particle type may be studied and the full interactions (scattering, decay, energy loss, path taken, etc.), are accounted for. The output of this simulation is a series of energy loss points which contain the amount of energy lost in  $keV/cm$  and the position in  $(x, y, z)$ .

Separate software tasks model the converting energy loss into electrons, the drifting of electrons, the avalanche process, and the electronics response.



Figure 3.21: A summary of all the effects modeled in the TPC MC simulation.

### 3.3.1 Drift Task

The drift task takes the energy loss points calculated from Geant4 and converts them into electrons. and then modeling their drift behavior in the field cage. As discussed previously the various processes[CITE To formula about drifting electronc]

A full microscopic treatment of the stochastic nature of each electron would be too cumbersome; most of the properties of the electrons are described by macroscopic quantities can be described by The charge of each MC point is converted to the total number of electrons liberated in the P-10 gas. This is a well understood property of proportional counters and is stable over a wide range of velocities and particle types [CITE BOOK]. The conversion factor of P-10 can be calculated by considering the partial volumes of each component of the gas. 3.3.

$$\text{Number of } e^- = 28 \text{ keV/cm} \quad (3.3)$$

### 3.3.2 Pad Response Task

After the avalanche process of the previous task, the total charge of the event is split over several pads defined by the Pad Response Function (as discussed in section ????). As shown in Fig. 3.22, there are three wires that lie directly above a given pad. The  $z$  coordinate of the avalanche can only be one of these three wires, where as the  $x$  coordinate can be any value along the wire. The



Figure 3.22: A cartoon of the wires over one pad.



Figure 3.23: Comparison of MC and data PRF

functional form of the software PRF (given in Eq. 3.4), was tuned to match the experimental data. Shown in Fig. 3.23, we see the tuned software PRF can match the experimental PRF from data over several crossing angles (as mentioned in Chapter ???? governs the shape of the PRF).

$$PRF(x, z) = \frac{1}{2\pi\sigma_z\sigma_x} \exp^{\frac{-(x-x_0)^2}{2\sigma_x^2}} \exp^{\frac{-(z-z_0)^2}{2\sigma_z^2}} \quad (3.4)$$

### 3.3.3 Electronics Task

The electronics task takes the total charge on each pad and simulates the electronics response, converting electronics into ADC channels. Accounting for the pedestal, the measured output in ADC channels (for a given gain setting) is given in Eq. 3.5.

$$1ADC = \frac{ADC_{Max} - ADC_{Pedestal}}{G * f_c} \quad (3.5)$$

### 3.3.4 Simulating Saturation

Add figure showing saturated time bucket spectra with location of saturation identified and with pulse shape from embedding I would like to add and how it blocks it. Add Figure with 2D pad

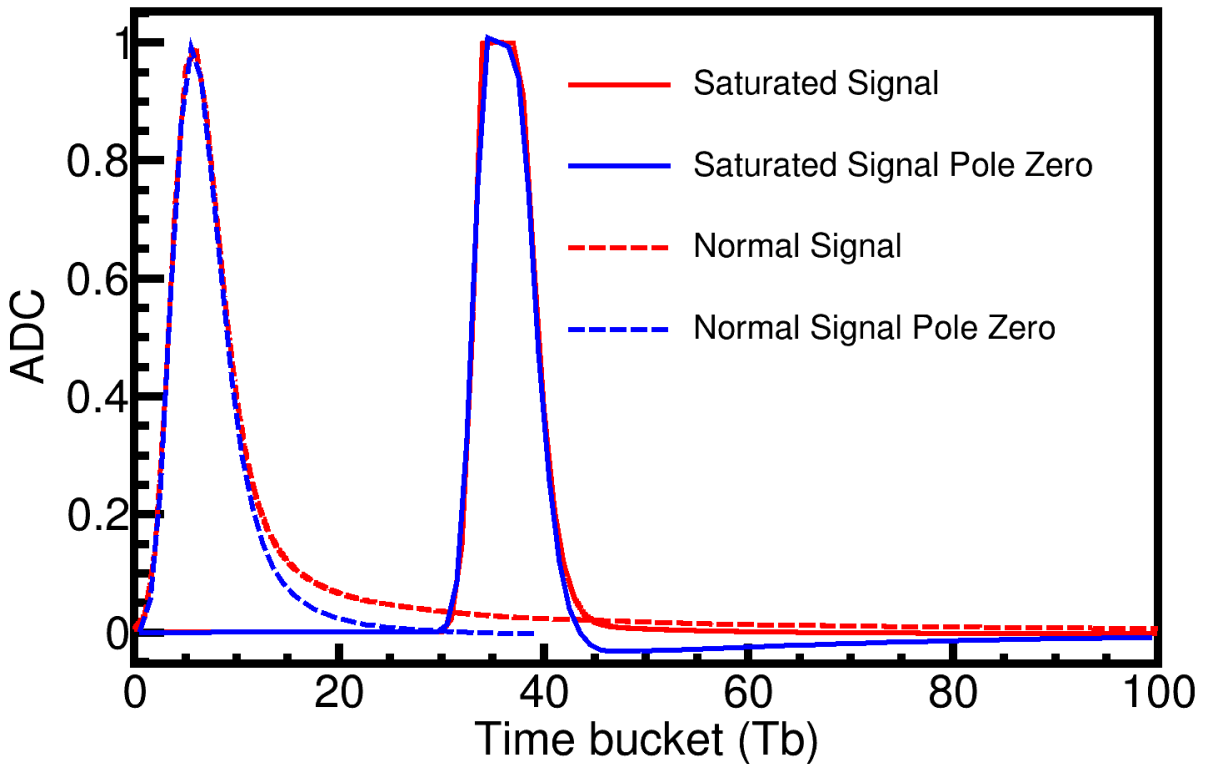


Figure 3.24: Pulse shapes for normal and saturated signals. Both are normalized to a max height of 1.

plane response with and without saturation flag

### 3.4 Monte Carlo Track Embedding

Add Figure of MC track embedding

Track embedding is the process of taking a simulated MC track from Geant4 and embedding its response into a real data event. After reconstructing this new embedded event we match the input MC track embedded to its corresponding final reconstructed track. By doing so we can evaluate the response of the entire TPC system to any given input value. The TPC system is composed of three major components (each which can introduce errors and or biases) the software, the detector, and the experimental setup.

As discussed in [SOFTWARE CHAPTER] the software is composed of several task, each

which introduce some error. Table REF TABLE] listing some of the errors each task may introduce illustrating how difficult propagating the errors would be through each system.

The detector system itself introduces errors related to the physical processes of the measurement itself. To address this we model the TPC (and its materials) in a Geant4 simulation which provides an accurate description of various interactions of a particle traversing the materials (including the gas volume) of the TPC.

software is the most straight forward; let the software routine process an input and measure the result. Understanding the measurement requires modeling the physics involved in the theory and operations of TPC's and the electronics. The experimental setup itself is quite large and complex, several ancillary detectors such as the Kyoto multiplicity array, Krakow veto array, Active veto array, beam identification detectors, etc. Even if a full accurate model could be constructed the complex trigger logic of the DAQ system would be impossible to model. If we notice that the biases and errors of the entire experimental setup is contained in the measured experimental data. Therefore, by inputting the MC data into a real experimental event (and measuring the output of that MC track) we can estimate the errors of the experimental setup.

The software analysis routine and the bias introduced by the trigger settings of the experiment introduce systematic errors in the reconstruction of tracks

### **3.4.1 MC and Data Comparison**

Add Figure of Pad response function for pion,proton.... for MC vs Data vs angles... Add Figure of Number of clusters of MC vs Data Add Figure of dEdx MC vs Data Add Figure of Momentum resolution MC vs Data Add Figure of track residuals? MC vs data?

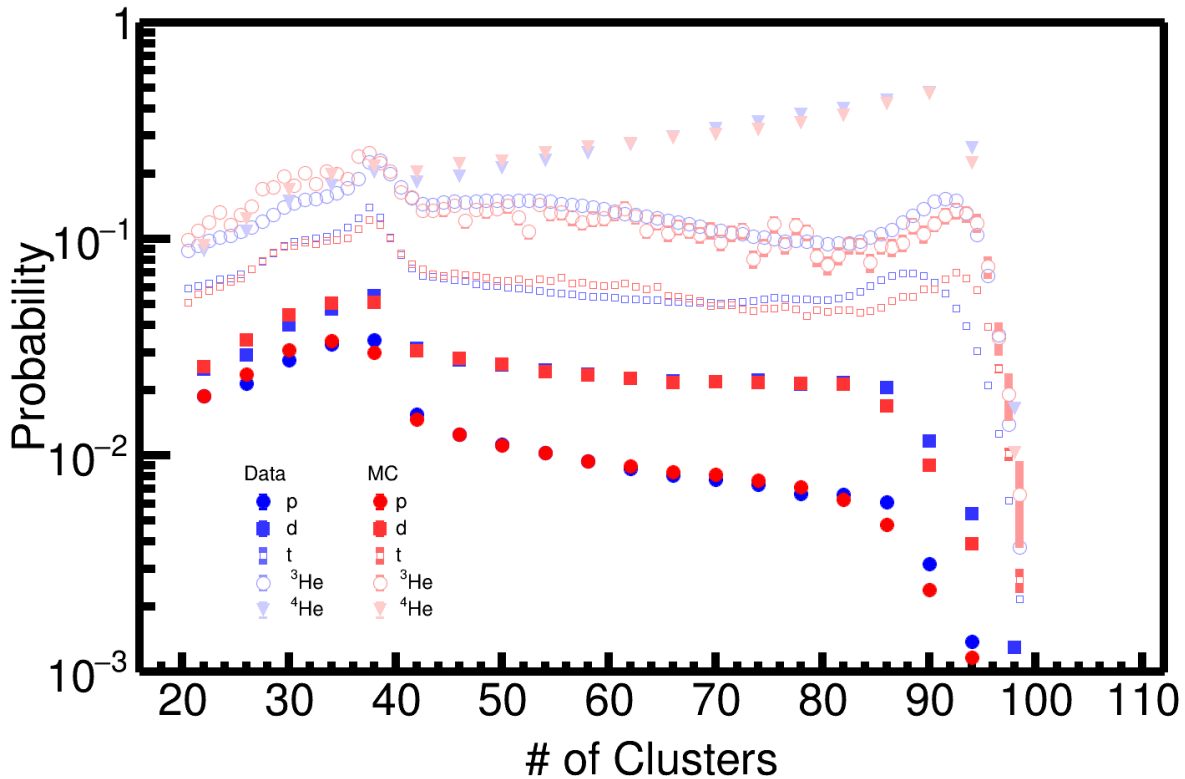


Figure 3.25: Comparison of MC to data.

### 3.5 Aligning TPC

### 3.6 CoBo timing correction

### 3.7 Efficiency Corrections

Add Figures of efficiency vs angles in TPC polar angle plot for pions

Since the S $\pi$ RIT TPC is a fixed target experiment it's angular coverage is certainly not  $4\pi$ .

Because the target is several cm away from the widow of the field cage the geometric acceptance is not even  $2\pi$ . The rectangular design complicates the calculation of the geometric acceptance, or the efficiency.

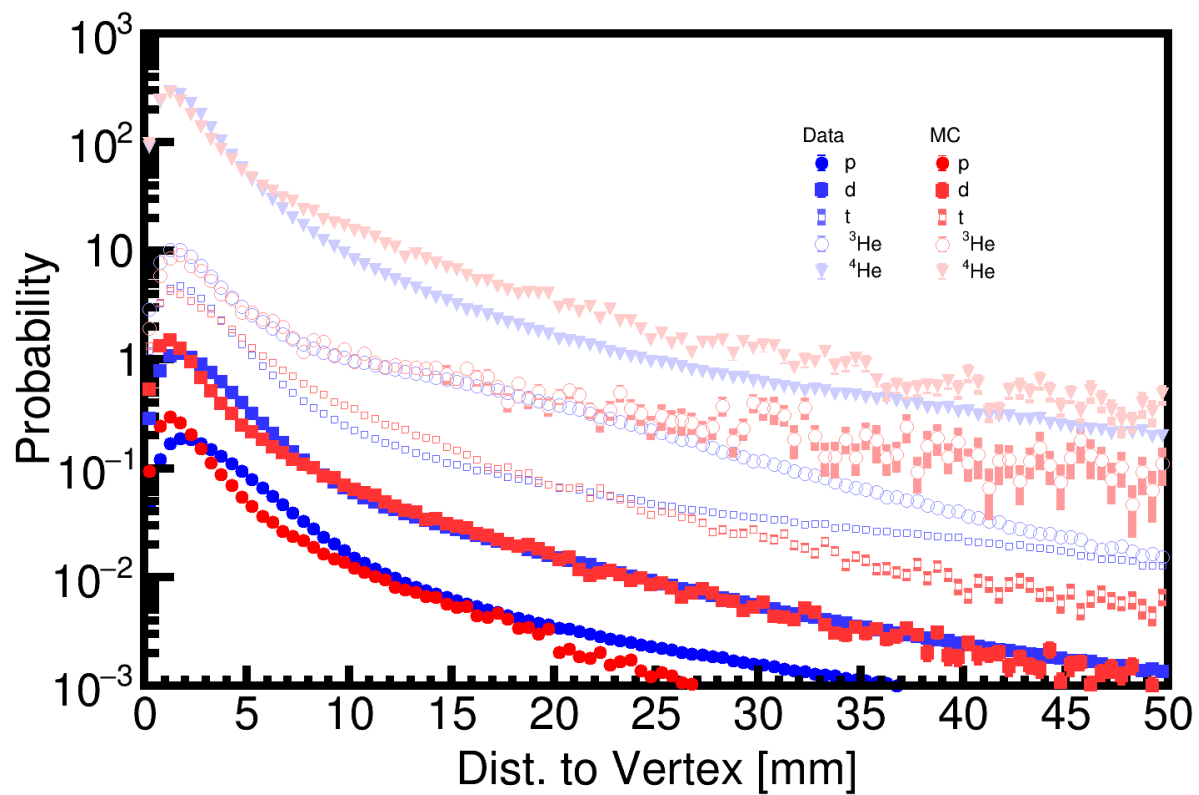


Figure 3.26: Comparison of MC to data.

### 3.8 Solid angle coverage

## CHAPTER 4

### DATA ANALYSIS II

#### 4.1 Beam Particle Identification

Figures of beam contaminants in our beam PID line. Table of beam purity reference to Jon's thesis paper

#### 4.2 Edge Cuts

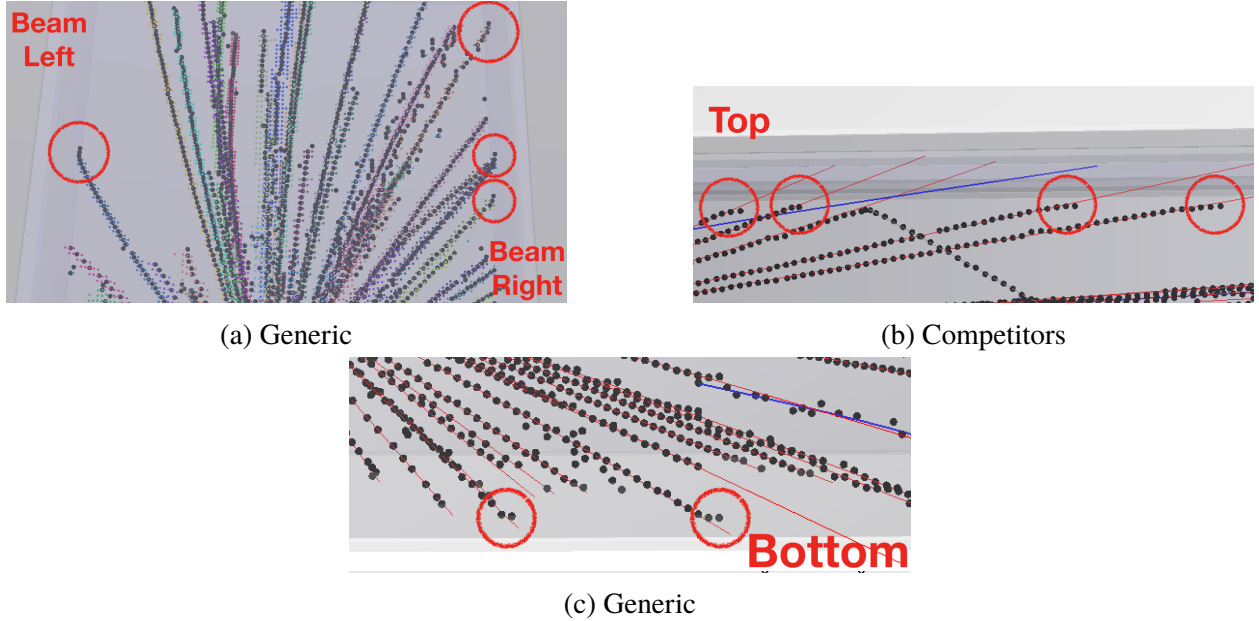
As seen in Fig. ??, edges of the measurement volume of the TPC we can see several edge effects distortion the clusters positions. The last pads on the edges of the pad-plane naturally have no neighbors on the outsides, therefore their cluster position is biased towards the inside of the TPC. Also since we measure a finite window in time for the vertical direction, pulses near the edge of the time-bucket window are clipped and the reconstructed times are biased towards inside the TPC volume.

The number of affected clusters is small, but the deviation at the end of the track is enough to start causing issues in the momentum reconstruction. Simple cuts around the left,right, top, and bottom of the TPC remove these clusters from the analysis,

$$|x| \geq 420 \text{ mm}, \quad y \leq -522 + y_0 \text{ mm}, \quad \text{and} \quad y \geq -64 + (\text{Hit Shift}) \text{ mm}.$$

#### 4.3 High Density Cut

The density of tracks near the target region is very high and most of electronics information from this region is inaccurate in both timing and charge value. Hits lying within an semi-ellipsoidal cut region around the target are removed from the software and not included in the track and momentum reconstruction.



Add picture of ellipsoid

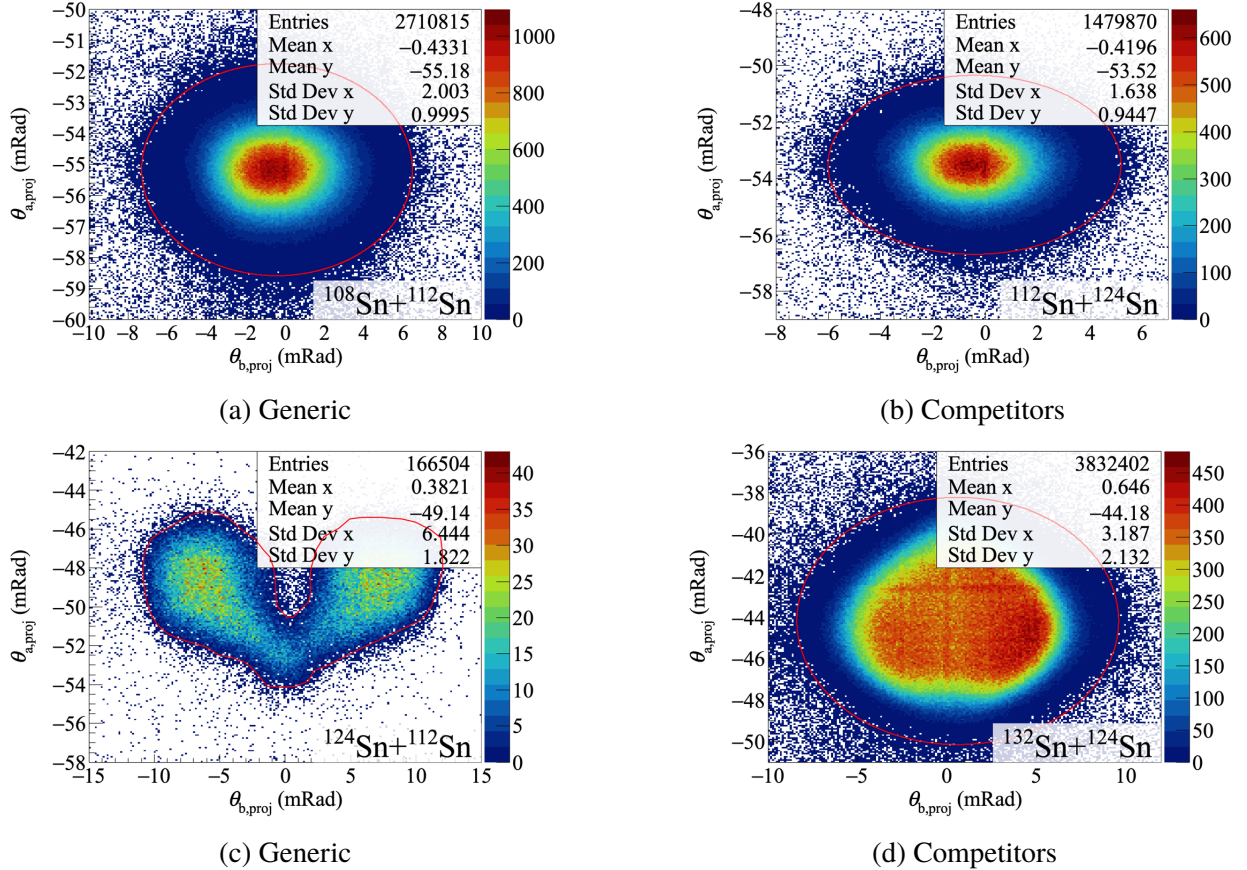
#### 4.4 Beam angle selection

The beam is bent by the magnetic field before hitting the target. The BDCs track the beam outside of the magnet. The beam is then propagated through the magnetic field until the target position.

The beam angle on target is categorized by two angles  $\theta_{a_{proj}}$  and  $\theta$

#### 4.5 Vertex Cut

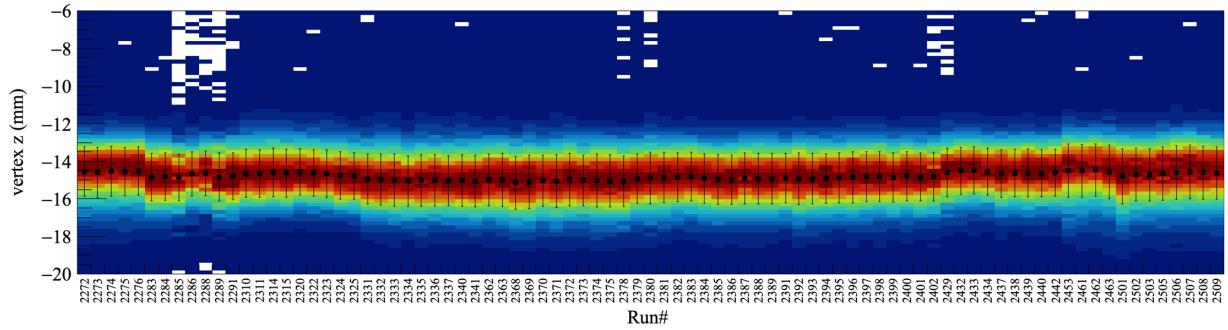
A vertex cut on vertices originating from the target region ensure we are selecting on nuclear collisions with the target. When looking at the z-component of the vertices of all events, we can see several features which correspond to different elements within the beam line and TPC. We also note that near the expected position of the target, WHAT POSITION??, we see a large enhancement of counts which corresponds to nuclear collisions on the target. The z-component of all runs in each beam type are plotted in the range of the target region in Fig. ???. Since the target thickness was less than 1 mm, the vertex resolution achieved can be experimentally measured by fitting the vertex



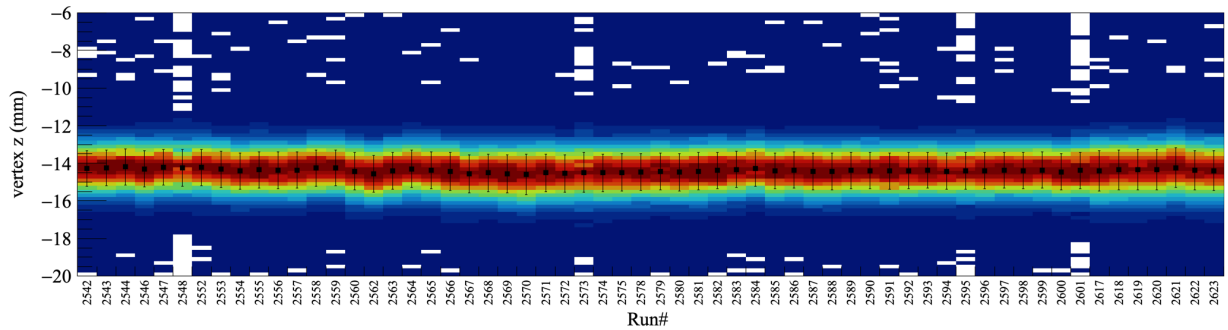
Vertex Resolution			
System	Mean (cm)	Sigma (cm)	
$^{132}\text{Sn} + ^{124}\text{Sn}$	-14.79	1.2	
$^{124}\text{Sn} + ^{112}\text{Sn}$	-14.71	1.1	
$^{112}\text{Sn} + ^{124}\text{Sn}$	-14.78	1.2	
$^{108}\text{Sn} + ^{112}\text{Sn}$	-14.75	1.3	

Table 4.1: Summary of measured vertices and their resolution.

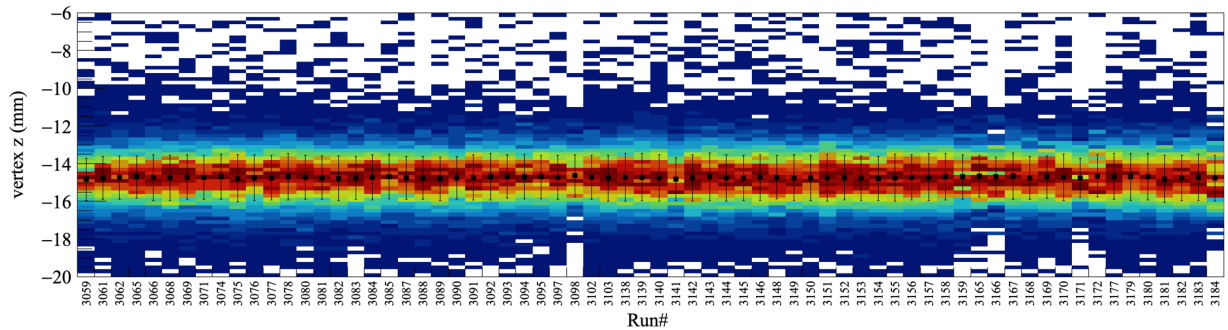
distribution, assuming a Gaussian distribution. The extracted vertex resolutions of each system are summarized in Table 4.1, with an average vertex resolution of 1.2 cm.



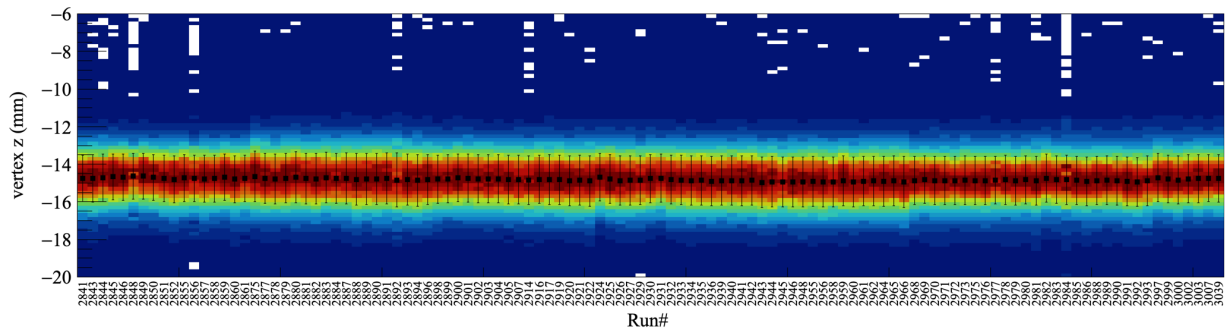
(a)  $^{108}\text{Sn} + ^{124}\text{Sn}$  vertex distribution for all runs.



(b)  $^{112}\text{Sn} + ^{124}\text{Sn}$  vertex distribution for all runs.



(c)  $^{124}\text{Sn} + ^{112}\text{Sn}$  vertex distribution for all runs.



(d)  $^{132}\text{Sn} + ^{124}\text{Sn}$  vertex distribution for all runs.

## 4.6 Impact Parameter Selection

The impact parameter which is defined as the distance (center-to-center), between two nuclei in a collision is a pure theoretical concept. Though experimentally there is no way in experiment to measure the impact parameter directly, several quantities have been indirectly related to the centrality of the collision CITE HERE. As discussed in Section CITE HERE, the Kyoto multiplicity array was used to experimentally trigger on central nuclear collision events. This is under the reasonable assumption that the number of charged particles in a collision grows as the impact parameter decreases. This is best described by a spectator-participant model of nuclear collisions, where a large fraction of the participating nucleons in the overlap region of the two colliding nuclei fragment into individual and clusters of nucleons. In the case where the impact parameter is zero, all the nucleons in both nuclei participate, were as larger impact parameters (peripheral collisions), less nucleons participate.

Certainly the Kyoto array introduces a bias in our measurement of the multiplicity of all the events. At low track multiplicities, the orientation of the event starts to play a major role. Theoretically the orientation of the event (the reaction plane) is random, but due to the fact that we only measure the multiplicity on the sides of the TPC, we are preferentially triggering on events with reaction planes that emit particles in these directions. Therefore events with low track multiplicity (therefore more peripheral), that emit preferentially up and down in the TPC will not be triggered on. This becomes less of an issue as even in mid-peripheral collisions were the number of particles emitted becomes much greater than the Kyoto multiplicity selection.

Assuming a geometric cross section  $\sigma$  and the impact parameter of the collision  $b$ ,

$$\sigma = \pi \cdot b^2, \quad (4.1)$$

we can estimate the maximum impact parameter  $b_{\max}$ , by measuring the total cross section of each system. A detailed analysis on determining the cross section is given in CITE HERE. I have summarized the finding of the cross section and  $b_{\max}$  for all the systems. Assuming  $b_{\max}$  represents

the most peripheral collisions we can define an estimate for the impact parameter  $\hat{b}$ , which we can define from the cumulative integral of the measured multiplicity distribution,

$$\hat{b} = b_{\max} \frac{\int_{\infty}^{M_x} f(M) dM}{\int_{\infty}^0 f(M) dM}. \quad (4.2)$$

## 4.7 Track Quality Cuts

In this section we will discuss the quality of the reconstructed track and will simply refer to it as the “track quality”. Certainly tracks with more clusters are of higher quality than those with few clusters. Occasionally the software will associate clusters and construct a track whose vertex does not coincide with the event vertex. This can occur for a variety of reasons. For a low momentum pion the radius of curvature is such that several rotations can occur in the event which the software can interpret as several tracks; while only one of the reconstructed track appears to originate from the event vertex. It could also happen that false tracks are created by the software from clusters which originate from several different real tracks. These are fairly obvious as they usually traverse the detector horizontally and the number of clusters is very low. In this situation the false track does not originate from anywhere near the vertex.

To reduce the number of fake tracks, or multiple counting of tracks, a simple cut on the measurement of a track’s distance to vertex can be used. The vector representing the minimum distance to vertex for each track can be calculated and its corresponding magnitude. We define the distance to vertex cut as a small sphere centered on the vertex location with a radius  $R$ . If the distance to vertex of a particular track  $d_i < R$  the track is assumed to have originated from the vertex; tracks that are outside are thrown out of the analysis.

Assuming tracks are mostly continuous in clusters, i.e. only randomly missing a few clusters, the number of clusters is directly related to the momentum resolution of a track.

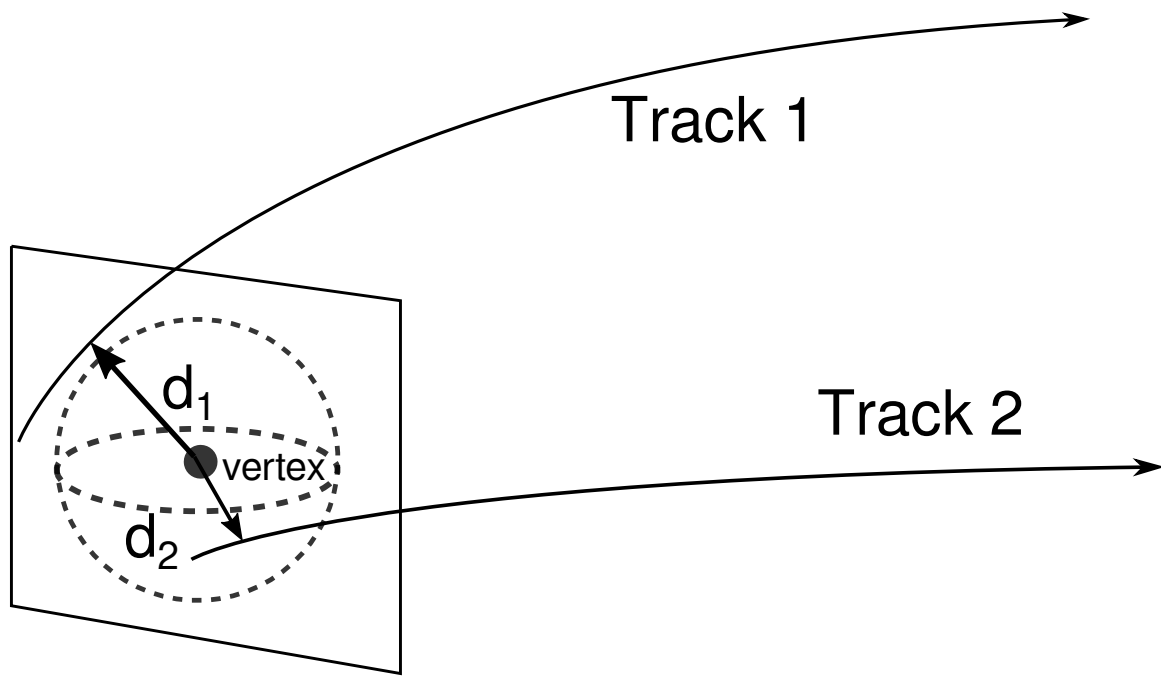


Figure 4.4: Distance to vertex for tracks.

#### 4.8 Angular Quality Cuts

## **CHAPTER 5**

### **RESULTS**

#### **5.1 Comparison to Theory**

Add figure of Pion spectra for different theory Reference paper for multiple theories

#### **5.2 Pion Spectra and Yields**

Add figure on Glauber model Add figure on comparison to FOPI data Add figure of angular coverage of TPC spectra

#### **5.3 $\pi^-/\pi^+$ Ratio**

Add figure of Theory for pion ratios

#### **5.4 Pion Double Ratio**

Add figure of Theory for pion ratios

#### **5.5 Pion Inferometry**

#### **5.6 Constraint on the Symmetry Energy**

maybe not...

## **APPENDIX**

## APPENDIX

### RUNS ANALYZED IN THIS DATA

System	#runs	Run numbers
$^{132}\text{Sn} + ^{124}\text{Sn}$	113	2841, 2843, 2844, 2845, 2846, 2848, 2849, 2850, 2851, 2852, 2855, 2856, 2857, 2858, 2859, 2860, 2861, 2875, 2877, 2878, 2879, 2880, 2881, 2882, 2883, 2884, 2887, 2888, 2889, 2890, 2891, 2892, 2893, 2894, 2896, 2898, 2899, 2900, 2901, 2902, 2903, 2904, 2905, 2907, 2914, 2916, 2917, 2919, 2920, 2921, 2922, 2924, 2925, 2926, 2927, 2929, 2930, 2931, 2932, 2933, 2934, 2935, 2936, 2939, 2940, 2941, 2942, 2943, 2944, 2945, 2946, 2948, 2955, 2956, 2958, 2959, 2960, 2961, 2962, 2964, 2965, 2966, 2968, 2969, 2970, 2971, 2972, 2973, 2975, 2976, 2977, 2978, 2979, 2980, 2981, 2982, 2983, 2984, 2985, 2986, 2988, 2989, 2990, 2991, 2992, 2993, 2997, 2999, 3000, 3002, 3003, 3007, 3039
$^{124}\text{Sn} + ^{112}\text{Sn}$	60	2542, 2543, 2544, 2546, 2547, 2548, 2552, 2553, 2554, 2555, 2556, 2557, 2558, 2559, 2560, 2562, 2563, 2564, 2565, 2566, 2567, 2568, 2569, 2570, 2571, 2572, 2573, 2574, 2575, 2578, 2579, 2580, 2581, 2582, 2583, 2584, 2585, 2586, 2587, 2588, 2589, 2590, 2591, 2592, 2593, 2594, 2595, 2596, 2597, 2598, 2599, 2600, 2601, 2617, 2618, 2619, 2620, 2621, 2622, 2623
$^{112}\text{Sn} + ^{124}\text{Sn}$	68	3059, 3061, 3062, 3065, 3066, 3068, 3069, 3071, 3074, 3075, 3076, 3077, 3078, 3080, 3081, 3082, 3083, 3084, 3085, 3087, 3088, 3089, 3090, 3091, 3092, 3093, 3094, 3095, 3097, 3098, 3102, 3103, 3138, 3139, 3140, 3141, 3142, 3143, 3144, 3145, 3146, 3148, 3149, 3150, 3151, 3152, 3153, 3154, 3155, 3156, 3157, 3158, 3159, 3165, 3166, 3167, 3168, 3169, 3170, 3171, 3172, 3177, 3179, 3180, 3181, 3182, 3183, 3184
$^{108}\text{Sn} + ^{112}\text{Sn}$	85	2272, 2273, 2274, 2275, 2276, 2283, 2284, 2285, 2286, 2288, 2289, 2291, 2310, 2311, 2314, 2315, 2320, 2322, 2323, 2324, 2325, 2331, 2332, 2333, 2334, 2335, 2336, 2337, 2340, 2341, 2362, 2363, 2368, 2369, 2370, 2371, 2372, 2373, 2374, 2375, 2378, 2379, 2380, 2381, 2382, 2383, 2384, 2385, 2386, 2387, 2388, 2389, 2391, 2392, 2393, 2394, 2395, 2396, 2397, 2398, 2399, 2400, 2401, 2402, 2429, 2432, 2433, 2434, 2437, 2438, 2439, 2440, 2442, 2453, 2461, 2462, 2463, 2501, 2502, 2503, 2505, 2506, 2507, 2508, 2509

Table .1: List of runs for the analysis.

**APPENDIX**  
**SECOND APPENDIX**

## **BIBLIOGRAPHY**

## BIBLIOGRAPHY

- [1] E. Gatti, et al., Optimum geometry for strip cathodes or grids in mwpc for avalanche localization along the anode wires, *Nucl. Instr. Meth. Phys. Res. A* 163 (1979) 83–92. doi:10.1016/0029-554X(79)90035-1.
- [2] W. Blum, W. Riegler, L. Rolandi, *Particle Detection with Drift Chambers*, Springer, Berlin, Heidelberg, 2008.
- [3] Y. Yano, The ri beam factory project: A status report, *Nucl. Instrum. Meth. B* 261 (1-2) (2007) 1009–1013. doi:10.1016/j.nimb.2007.04.174.
- [4] T. Kobayashi, et al., Samurai spectrometer for ri beam experiments, *Nucl. Instrum. Meth. B* 317 (2013) 294–304. doi:10.1016/j.nimb.2013.05.089.
- [5] E. Pollacco, et al., Get: A generic and comprehensive electronics system for nuclear physics experiments, *Physics Procedia* 37 (2012) 1799–1804. doi:10.1016/j.phpro.2012.02.506.
- [6] M. Al-Turany, et al., The fairroot framework, *J. Phys.: Conf. Ser.* 396 (2). doi:10.1088/1742-6596/396/2/022001.
- [7] C. Höppner, et al., A novel generic framework for track fitting in complex detector systems, *Nucl. Instrum. Meth. A* 620 (2-3) (2010) 518–525. doi:10.1016/j.nima.2010.03.136.
- [8] W. Waltenberger, Rave—a detector-independent toolkit to reconstruct vertices, *IEEE Transactions on Nuclear Science* 58 (2) (2011) 434–444. doi:10.1109/TNS.2011.2119492.
- [9] G. Rai, et al., A tpc detector for the study of high multiplicity heavy ion collisions, *IEEE Transactions on Nuclear Science* 37 (2) (1990) 56–64. doi:10.1109/23.106592.
- [10] S. Collaboraiton, Samurai dipole magnet field map (2020).  
URL <https://ribf.riken.jp/SAMURAI/index.php?Magnet>
- [11] G. Van Buren, et al., Correcting for distortions due to ionization in the star tpc, *Nucl. Instrum. Meth. A* 566 (1) (2006) 22–25. doi:10.1016/j.nima.2006.05.131.